LDRD final report for "Tactical laser Weapons for Defense" SI

R. Beach and L. Zapata

January 30, 2002

DISCLAIMER

January 30, 2002

To: **Rokaya A. Al-Ayat**
From: **Ray Beach and Luis Zapata**
Subject: **LDRD final report for "Tactical laser Weapons for Defense" SI**
            (Tracking code 01-SI-011)

The focus of this project was a convincing demonstration of two new technological approaches to high beam quality; high average power solid-state laser systems that would be of interest for tactical laser weapon applications. Two pathways had been identified to such systems that built on existing thin disk and fiber laser technologies. This SI was used as seed funding to further develop and vet these ideas. Significantly, the LLNL specific enhancements to these proposed technology paths were specifically addressed for devising systems scaleable to the 100 kW average power level. In the course of performing this work we have established an intellectual property base that protects and distinguishes us from other competitive approaches to the same end.

The interest and motivation to press forward with laser weapons is emerging as a compelling national need, as articulated in a report recently issued by the High Energy Laser Executive Review Panel (HELERP). The HELERP report addresses near-term needs, strategic vision, and programmatic balance for a vibrant national effort in laser weapons. Solid-state lasers are, for the first time, being actively considered as a candidate for the KILL weapon; (solid state lasers have previously only regarded in supporting roles for tracking the missile and for atmospheric correction.) Perhaps most importantly, this national committee has affirmed that laser weapons are to play a critical tactical role for the warfighter in the 21st century. The key attributes of HEL weapons (not otherwise available) are the ability: to engage high-speed maneuverable targets with short reaction time, and to provide graduated (less than lethal) effects when required. It is exciting for LLNL laser physicists that solid-state laser weapons have received, for the first time, the same level of stature as that of chemical lasers, upon which such major national efforts as the Air Borne Laser (ABL), Space Borne Laser (SBL), and Tactical High Energy Laser (THEL) are based. LLNL has long advocated solid-state lasers as the approach of choice, and has a strong infrastructure in optical design, thermal management, and diode laser arrays. The research that we have performed under this program has been instrumental in establishing LLNL in the developing field of tactical laser weapons.

The following reports cover in detail the work that has been done to further both the thin disk and fiber approaches that were investigated in this SI:
  * Section I - Thin Disk HiBriTE Laser Weapon
  * Section II – Ribbon Laser Weapon
  * Section III – Manuscript accepted for publication in JOSA B entitled, "Scalable Antiguided Ribbon Laser Concept"

Section I - Thin Disk HiBriTE Laser Weapon: The thin-disk laser can be operated in a continuous mode, and may also offer favorable attributes in efficiency and weight for the weapon system. We refer to our composite thin-disk Yb:YAG laser as the HiBriTE ("High Brightness Tactical Engagement") Laser Weapon. We believe this approach is a breakthrough for scaling solid-state lasers to extremely high average power. Figure 1 depicts the essence of the thin-disk approach. Because the edges of the sample become negligible (due to the "thinness"), the dominant heat flow direction is aligned with the laser beam propagation direction. In the ideal case, where the thermal gradients are parallel to the propagation direction, the gradients do not impart any phase distortion across the laser beam aperture. Additionally, because the fracture-limited thermal power varies inversely with its thickness, the thin-disk laser can scale to very high average power (since the Yb:YAG thickness is <200µm) . Our intense interest in the HiBriTE

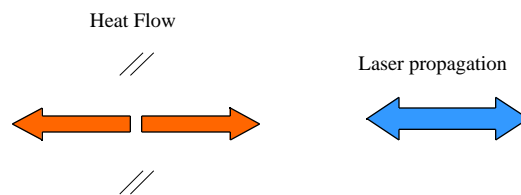Heat Flow

Laser propagation

Figure 1. Thin disk of laser material in which the heat flows parallel to the laser beam propagation direction.

laser concept is predicated on its potential to offer extremely high average power, together with high beam quality.

Today, the dominant development of this type of laser is being pursued at the University of Stuttgart in a group headed by Prof. Adolf Geissen, where it is used as a high power laser for material processing. The thin disk configuration has recently been demonstrated at cw output powers exceeding 1 kW with the promise of very high beam quality. The fundamental idea of the Stuttgart approach, which enables the generation of high average power with high beam quality, is illustrated in Fig. 2. Stuttgart scientists have developed multi-pass pump geometries to accommodate the use of thin disks, which implies very short absorption distances for the laser diode pump light. Figure 2 shows the original multi-pass pump geometry employed by the Stuttgart group. Here, the pump beam is re-imaged through the sample more than 16 times to increase the net absorption path. More recent versions employ a parabolic reflector to simplify the pump geometry. The very complicated pump geometry, and the obvious limitations to power scaling that it imposes, are issues that the proposed thin disk concept (HiBriTE) explicitly recognizes and addresses.

Laser resonator mirrors
Pump reflector mirrors
Pump light injection
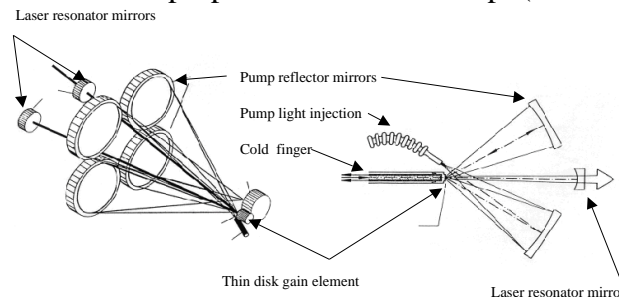Cold finger
Thin disk gain element
Laser resonator mirror

Figure 2. Thin disk geometry developed by the Stuttgart group in which the pump radiation is multi passed through the thin disk sample to increase absorption.

Figure 3 depicts our enhancement of the composite thin-disk approach, (together with Geissen's original geometry). At the top of the thin-disk gain-loaded Yb:YAG layer there is an index matched undoped cap, attached using diffusion bonding technology. The purpose of the undoped cap is three-fold:

- It enables side pumping of the thin disk by guiding the pump light. The pump geometry is greatly facilitated by edge-pumping the gain sample using non-imaging lens duct technology, in contrast to the complicated re-imaging method of Geissen.

- Amplified Spontaneous Emission (ASE) as well as parasitics are suppressed by more than 10x. The ASE impact is minimized because the optically-passive undoped YAG cap volume adjacent to the Yb:YAG thin gain-sheet drastically reduces the solid angle over which fluorescence is trapped by total internal reflection.

- The composite thin-disk laser geometry adds strength – in proportion to the cube of its thickness – to the otherwise fragile thin-disk, resisting the effects of thermally induced deformations currently imposing the main wave front errors in these devices.

Undoped YAG
Pump
Lase
Pump
Yb^{3+}:YAG   Heat
HiBriTE
Laser

Pump & Lase
Yb:YAG
Heat
Geissen's
Approach
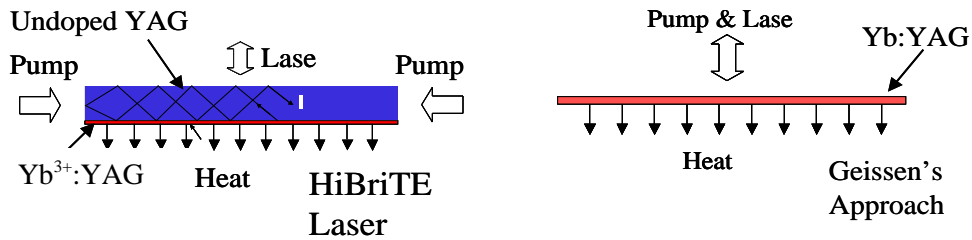
Fig. 3: Comparison of thin-disk laser approaches.

Finally, it is crucial to recall that the diffusion bonded undoped cap does not compromise the thermal advantage of the thin Yb:YAG portion. The cap simply rises to a uniform, constant temperature, a benign effect which does not affect the thermal gradients in the thin-disk.

Figure 4 depicts the design of our first generation prototype composite thin-disk laser. The "enabling" technologies shown in Fig. 4 are the Yb:YAG / YAG composite laser disk; the diode arrays, radiance conditioned by micro-lenses and hollow lens ducts to match the numerical aperture of the composite; the high performance mini-channel cooler; the thin-film coating; and the telescopic resonator (not shown). The HR coating on the YAG gain element will transport a heat flux of up to 500 W/cm^2 in the present device (1.5 kW/ cm^2 desired for future devices). We expect to minimize the thermal impedance of our coating formulation by using dense, low porosity coatings presently produced by ion-assisted DC magnetron sputtering. We also have demonstrated high beam quality using a telescopic resonator (not shown).

ü HEL thin-film coating

dielectric HR + gold
indium solder
cooling μ-channels

200 μm Yb³⁺:YAG 1.3 mm cladding
pump delivery

ü High perfomance μ-channel cooler

laser beam

low Fresnel number resonator

concentrator

YAG / Yb:YAG composite thin disk

heat flow

ü High power diode arrays

ü Diffusion bonded Yb:YAG/YAG thin -disk
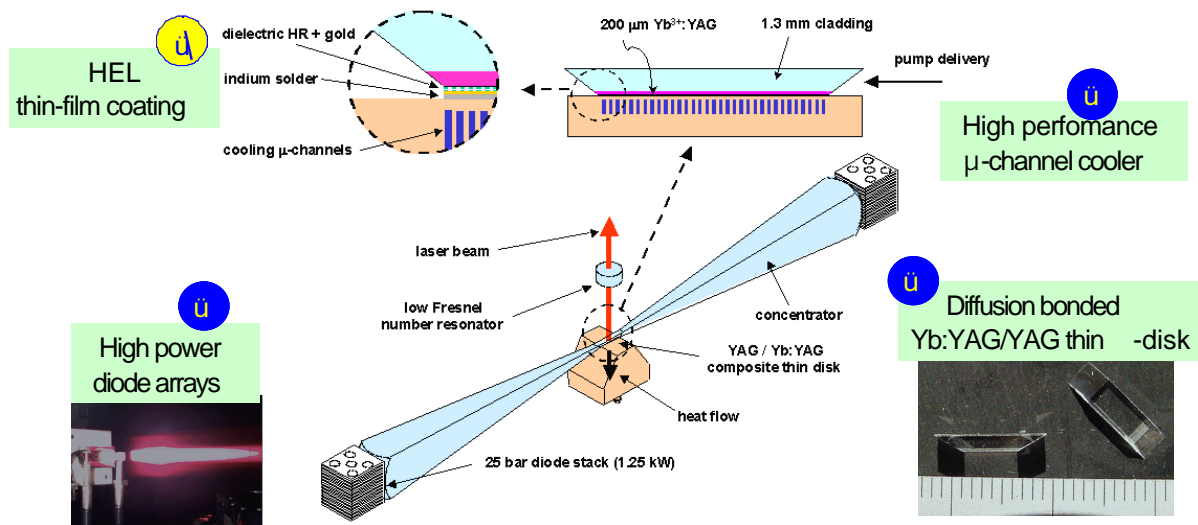
25 bar diode stack (1.25 kW)

Figure 4. Our thin disk concept uses an undoped cap diffusion bonded to the highly-doped Yb:YAG thin disk layer. The enabling technologies with blue check marks have performed as desired in our tests and appear ready for scaling. We are focusing on producing HR coatings of low thermal impedance compatible with indium soldering.

Scaling the HiBriTE laser to enormous power is in principle graceful – it is accomplished by proportionally increasing the aperture diameter, undoped cap thickness, and diode array size – while keeping the thin Yb:YAG gain layer thickness *constant*. This proportional scaling results in a constant temperature gradient and gain coefficient in the dimension parallel to the beam. Therefore, a small composite thin-disk device has similar operating parameters of laser gain, surface heat intensity, and thermal stress for the geometrically similar scaled-up version. In contrast, ASE and resonator performance are more sensitive to the scale of the module being tested. We estimate that the ASE-limited-aperture is about 12 mm in diameter. Monte-Carlo ray tracing techniques are typically employed to assess ASE intensity growth and gain depletion. This approach has proved useful in the design of ASE limited glass slabs used in laser fusion research. Thus far, our calculations indicate that a hexagonal gain element with canted sides provides for the best suppression of parasitics and ASE, offering about 8 kW in power.

Figure 5 contains our design for an ASE-limited 8 kW hexagonal aperture on the left, and the vision of how to scale the laser to 100 kW on the right. Shallow "grooves" cut *only* into the thin Yb:YAG gain-sheet isolate the individual gain regions (12 mm across in size). The ASE-limited apertures (delineated by the grooves) are patterned into a closely packed honeycomb so that the 100 kW aperture can be extracted with high fill and low loss by employing a telescopic resonator. The telescopic resonator can provide a large, transverse single mode that can be made to match large apertures – the principal means of thin-disk scaling. It is also a straightforward task to configure a telescopic resonator for stability (rather insensitive to fluctuations) and usefully, it can be adjusted to compensate for the expected (mostly spherical) thermal deformation. Our direction in this area includes the development of a more compact telescopic resonator based on aspheric optics.
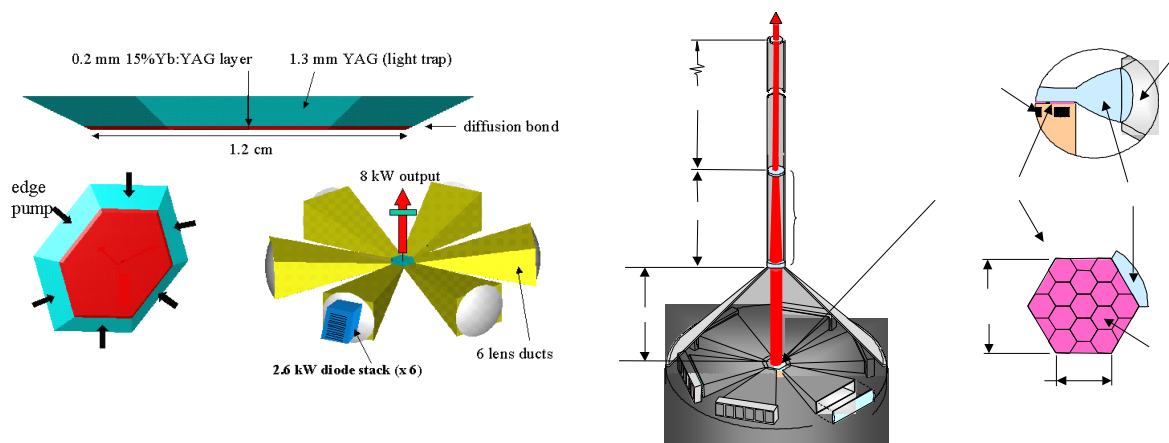
Figure 5: LHS: The 8 kW device has a hexagonal shape with the gain medium (in red) bonded to a disk of the same shape and index of refraction (in light blue). Diode stacks from six sides provide a total of 18 kW of optical pump power. RHS: Vision of 100kW weapon based on tiling numerous 8 kW apertures.

Considerable progress has been made this last year. Hardware was designed, built and successfully activated. A picture of this hardware in the experimental set up is shown in the LHS of Fig. 6. During initial operation at low duty factor (1 ms pulses at 1 to 10 Hz) a stable, multi-mode resonator was used to collect slope efficiency data (laser output vs. input energy) for several concave (R = 2 m) output couplers. The output power optimized with the 91% reflector (see the graph in the RHS of Fig. 6). We will use these data to compare with our energetics codes predictions.
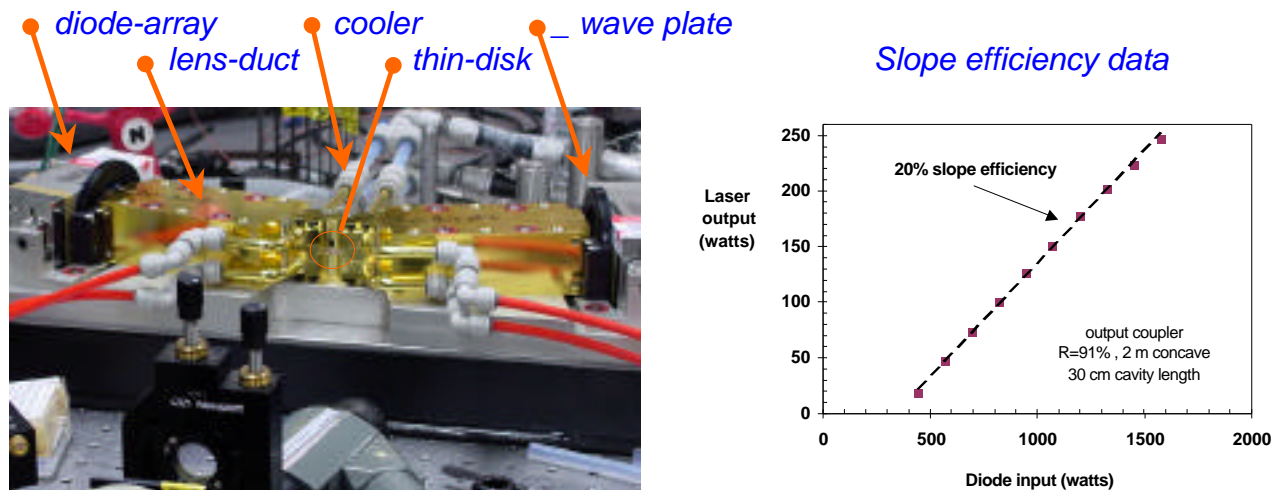
Figure 6: The new hardware saw "first light" during the last week of 2001. Initial activation at low duty in a stable resonator configuration produced slope efficiency data for several output couplers.

The design emphasizes thermal management predicated on indium soldering the thin-disk gain medium by its thin-film HR mirror to a high performance cooler of mini-channel design. The new hardware incorporates improvements in diode pump delivery, and cooling capacity. The precision alignment of the pump delivery parts – critical to the performance of the device – was easily accomplished because metal surfaces register

each other via a common assembly plate. Thus, all parts were pre-aligned by machined stops before assembly and no adjustments were required. The integrity of our "high value" thin-disk laser gain component is protected in this design. Once soldered to the cooler, it is mated with the lens-duct ends, which utilize a cooler surface for reference. The ensemble is then mated in the assembly plate to the larger pump delivery hardware.

We have completed the following milestones:

- *Milestone 1: Develop and fabricate composite Yb:YAG laser disks with dielectric / metallic coating which meets specifications*
  - A suitable HR coating on the YAG/Yb:YAG composite gain element has been developed after many iterations. The sequence for the final prescription is: plasma etch of YAG substrate / nine SiO_2-Ta_2O_5 layer-pairs for HR / plasma etch in O_2 / $/2$ layer of Al_2O_3 / plasma etch in O_2 / Cu (300 nm) for wide-angle pump field reflection / Ni for indium barrier (1,000 nm) / Au alloying agent (300 nm) / In soldering agent (4-10 µm).
  - Six Yb:YAG / YAG composite slabs which adhere to specifications have been procured from Onyx Optics and are available for soldering to chillers (Fig. 7).
  - Precision indium soldering method was developed.

Figure 7: A fully coated thin-disk on the left and after soldering

Milestone 2: Develop and fabricate laser disk cooler capable of extracting 300 W/cm^2 of heat.

  - The high-performance chiller has been designed and fabricated using wire-EDM to cut 125 µm channels with 50% fill factor (see Fig. 8 below). A method was developed to assure the adhesion of nickel to the Cu/W chiller based on an acidic etch of the metal surface (to eliminate copper globules formed in the polishing step). High reflectivity gold was then electroplated onto the nickel layer. We elected to employ Cu/W metal because it is nearly exactly expansion-matched to the YAG gain element and therefore should be superior for high power performance.
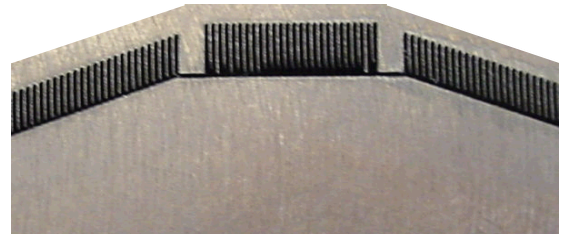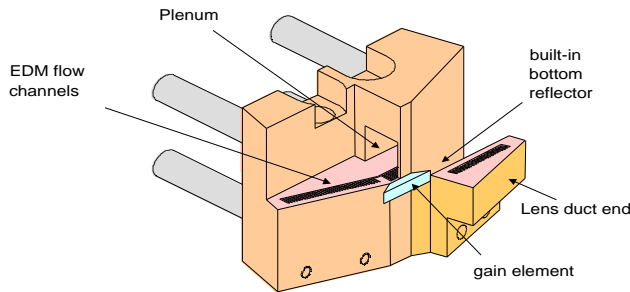
Figure 8. LHS: Schematic of cooler, revealing cooling channels, composite thin-disk crystal, and plenums. RHS: Photo of the cooler. A wire EDM approach has been employed to produce 125 μm channels, which cool the thin disk crystal and the ends of the lens ducts.

❓ *Milestone 3: Complete hollow lens duct hardware and operate telescope*
   ❓ The pump delivery hardware has been designed and fabricated, such that the hollow lens duct is integral with the Yb:YAG chiller (i.e. comprises one of its sides). The pump light enters the gain medium at a 15° angle to optimize the transmission through the Brewster angle windows of the gain element.
   ❓ We demonstrated the functionality of the telescopic resonator showing that the mode could be controlled to be TEM_{00} (or TEM_{0N}) by adjusting the fundamental beam waist on the gain element (Fig. 9).
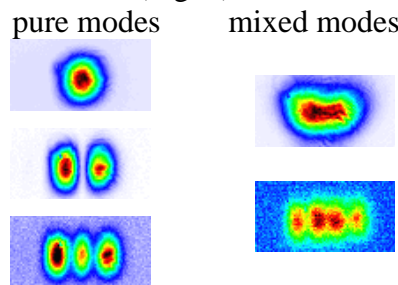
Figure 9: Example of controlled production of low order transverse mode using telescopic resonator.

   ❓ A low-power single line probe laser has been set-up for measuring the wave-front, gain, and temperature of the composite disk, (example of temperature data in Fig. 10)
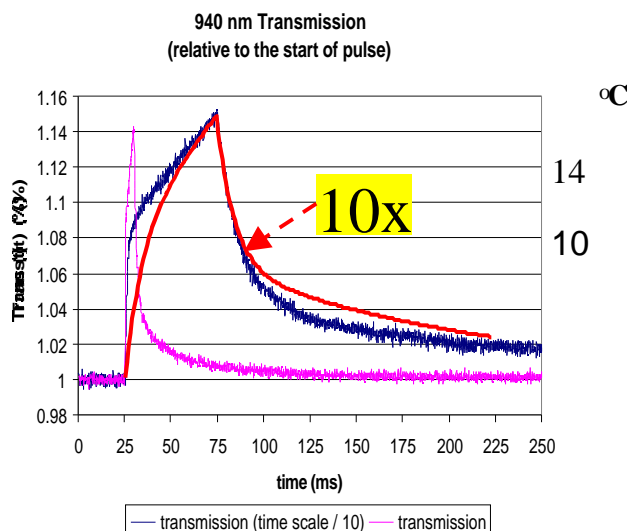
Figure 10: Example of temperature as a function of time (notice use of expanded scale). The 940 nm probe laser transmission (y-axis on the left) is sensitive to the temperature of the Yb:YAG gain-volume. The probe interrogates the dynamics of the populations (which is reflected in the temperature). The long decay (magenta) is caused by the cooling rate through the HEL coating.

- *Milestone 4: Demonstrate integrated low duty factor laser output*

    - Align diode stacks / lens ducts / laser disk.
    - Image laser fluorescence due to side-pumping with scientific CCD. Compare fluorescence data to ray-trace models.
    - Perform low duty factor laser experiments with stable resonator.
    - Compare data to laser energetics model, and optimized output coupler.
    - Evaluate properties of telescopic resonator
    - Validate telescopic resonator codes by comparing prediction with beam quality measurements

  (Experiments marked ? are planned for execution under DoD support).

- We expect to achieve our objective of 300 W (Milestone 5) with 1-2 months.

Section II – Ribbon Laser Weapon: This effort has been focused on defining a new power-scalable concept for fiber lasers known as the Ribbon Laser. The strategy for scaling is to include numerous cores in a single fiber, each able to deliver a certain amount of power (eventually about 100- 200 W). The key, of course, is to maintain a phase-locked wave front across these numerous core regions.

     A simplified drawing of our new Ribbon Laser appears in Fig. 11, where a transverse profile (perpendicular to the fiber and along the long axis) is shown. In this example, the refractive index is plotted, and it is seen to vary periodically. The two main approaches for achieving phase-locking are based on: evanescent and radiative coupling. As can be seen from the figure, if the effective index of the propagating mode is intermediate between the low and high indices, then the coupling is evanescent (i.e. the "tails" of the neighboring fields in each of the cores overlap). If the effective index is lower, then the field is not confined and migrates freely throughout the entire Ribbon structure.
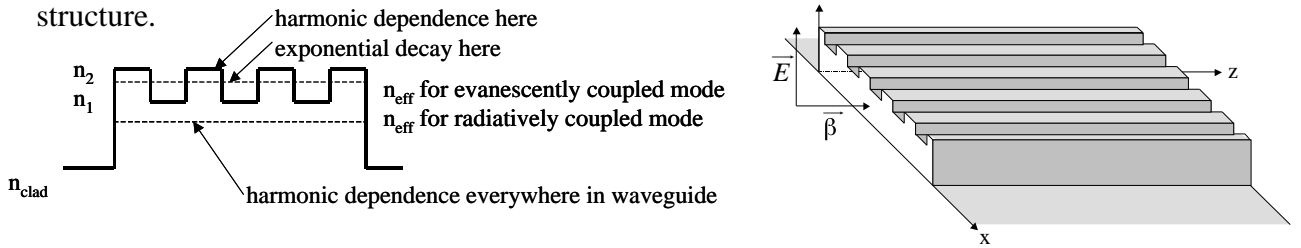
Figure 11: LHS: Simplified drawing of the transverse Ribbon Laser structure, showing the modulated refractive index, and the n_{eff} values that give rise to evanescent and radiatively coupled modes. RHS: Three dimensional drawing of E-field, propagation direction (β), and refractive index.

     We have found that a "photonic bandgap" emerges in this structure, depending on the sense of the refractive index variation. In Fig. 12 below, we see that the gain regions are the same in the upper and lower plots, although the modulation of the index has an opposite sign. On the LHS, the overlap for each of the modes is plotted against the effective index, while the field characterizing the two modes on each side of the bandgap are expressly shown on the RHS. It is readily apparent that the bandgap is analogous to the valence and conduction bands of a crystal.

Figure 12: Plots of the overlap of the field with the gain regions, against the effective index of the modes. The field intensities for the two modes at the "photonic bandgap" are plotted on the right.

The most interesting result that we obtained is pictured below in Fig. 13. Here we utilize a constant index across the Ribbon Laser, and observe that the mode structure leads to the dominance of a single mode that has considerably more overlap than all the other modes. Of course the greater o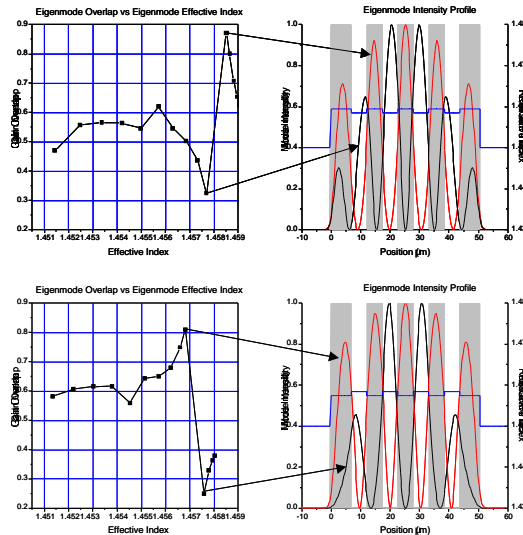verlap of this mode leads to much higher gain, such that it becomes the preferred operating mode of the laser. The preferred mode exhibits five intensity peaks, one within each of the gain regions. All of the other modes have more or less than five intensity lobes, so they have less overlap with the gain regions. This type of structure, based on having a uniform index across the ribbon structure, is analogous to a "photonic metal," since the uniform refractive index is like the constant potential seen by electrons in a metal.
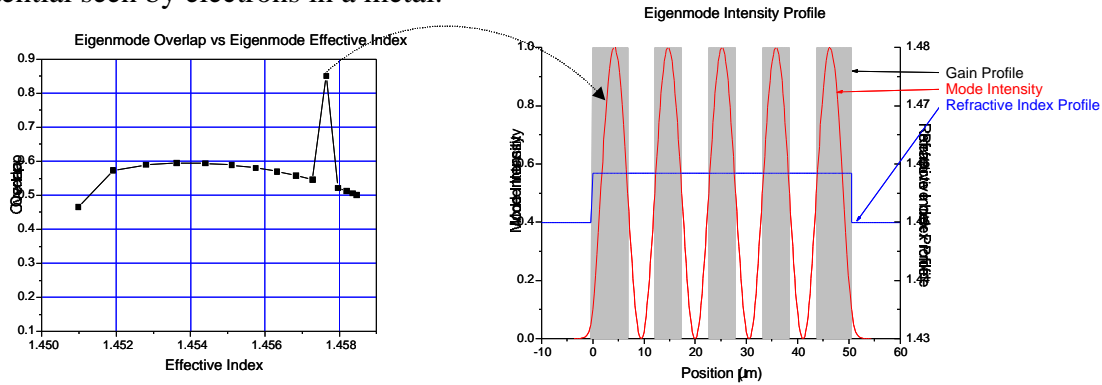
Figure 13: Predicted modal structure for 5-core Ribbon Laser, based on a uniform transverse refractive index profile. A single preferred mode emerges that has significantly more overlap (and gain) than the other modes.

In collaboration with Schott Glass Technologies and Collimated Holes, we have produced a first prototype of the Ribbon Laser structure (should below in Fig. 14). While the index control is barely acceptable at this juncture, the device has exhibited a reasonable level of coherence to suggest that our theory of the Ribbon Laser is viable. The fiber is based on Nd-doped LG-660 laser glass; the outer undoped region is the pump clad area (where the diode pump light is introduced), while the alternating doped and undoped sections appear as the rectangular core region (having roughly the same refractive index).
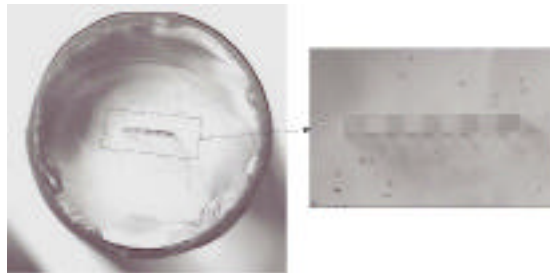
Figure 14: Photograph of the first prototype Ribbon Laser, showing the outer pump clad, and the alternating Nd-doped and undoped regions.

The prototype Ribbon Laser exhibited slope efficiencies of up to 20 %, and noted in Fig. 15. The laser operated near 1.05 μm as expected, and was pumped near 0.808 μm. Also featured in Fig. 15 (RHS) are measurements of the coherence exhibited by the device. In these experiments, two of the various cores (numbered 1 through 5) are arranged to interfere – the depth of the modulation or the visibility of the fringes is seen to vary from 39 % to 13 %. With improved index control, we expect to attain the full level of modulation.
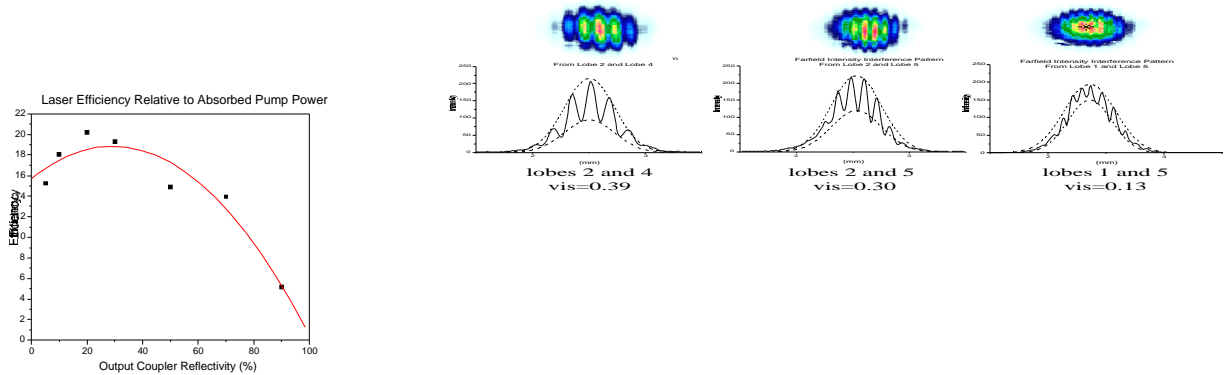
Figure 15: Experimental data obtained from the first prototype Ribbon Laser, including slope efficiency data and measurements of the finge visibility (coherence) between pair of cores).

At this juncture, we have completed our theory of the Ribbon Laser and have demonstrated that the first working prototype has properties consistent with predictions. With these initial results we are encouraged that the Ribbon Laser concept is scalable, and could one day reach power levels consistent with laser weapons.

Scalable Antiguided Ribbon Laser Concept

Raymond J. Beach, Michael D. Feit, Ralph H. Page, LeAnn D. Brasure, Russell Wilcox, and Stephen A. Payne

April 30, 2001

U.S. Department of Energy

Lawrence
Livermore
National
Laboratory

DISCLAIMER

Scalable Antiguided Ribbon Laser Concept[1]

Raymond J. Beach, Michael D. Feit, Ralph H. Page, LeAnn D. Brasure, Russell Wilcox,
and Stephen A. Payne
Lawrence Livermore National Laboratory, PO Box 808, Livermore, CA 94551

Abstract
A new scalable fiber laser approach is described and modeled, based on phase-locking
multiple gain cores in an antiguided structure. In essence, the waveguide is comprised of
a periodic sequence of gain-loaded and no-gain segments having uniform refractive index
(referred to as the "ribbon") encapsulated within a reduced index cladding region. Our
calculations reveal that the constant index profile within the ribbon structure provides
optimal mode discrimination; the refractive index must be constant within ~±0.001 to
ensure single-mode operation for a 5-core design. One-dimensional and two-dimensional
calculations are pursued to support the design criteria. Slight periodic variation in
refractive index of the ribbon laser lead to the emergence of a photonic bandgap, in
analogy to so-called "holey fibers". Our constant index design, together with the periodic
gain profile, may be described as a photonic metal.

Scalable Antiguided Ribbon Laser Concept

Raymond J. Beach, Michael D. Feit, Ralph H. Page, LeAnn D. Brasure, Russell Wilcox,
and Stephen A. Payne

Lawrence Livermore National Laboratory, PO Box 808, Livermore, CA 94551

1. Introduction

This paper describes a new, robustly scalable technique for phase locking multiple gain cores in a fiber structure based on anti-guiding or radiative coupling.[1] Our focus is on a ribbon-like geometry in which the waveguide region contains multiple gain cores alternating with non-gain regions in a periodic array. An outer, lower index cladding surrounds the entire ribbon structure. The distinguishing feature of our design is a constant refractive index profile across the waveguide region as opposed to alternating higher and lower index regions. Our modeling predicts the constant index design will provide modes that meet our two critical design requirements: strongly favored oscillation in a single transverse mode and good intensity uniformity across the waveguide structure. Interestingly when the index profile is allowed to have a small index variation the model predicts formation of bandgaps in the allowed wave vector values. Essentially, the ribbon fiber has a similar structure to that of photonic crystal fiber designs.[2]

Because the ribbon structure described in this paper contains a waveguiding region embedded in a lower index outer cladding region, it has many features in common with single-core double-clad fiber lasers. The development of these double-clad fiber lasers has brought fiber lasers to the forefront of possible approaches for high beam quality, high average power continuous-wave laser sources. However, there are drawbacks to the implementation of a fiber-based system that the design described within should address. Individual fiber cores are believed to be limited to roughly 100 W of average power generation[3,4,5] due to the output facet damage limit, therefore very high average power fiber systems are anticipated to require phase combining many individual apertures. The anti-guiding design will allow the radiation output of the multiple cores to stay coherently phased together even as the number of cores increases. Conceptually, the device could be scaled to higher powers simply by increasing the number of anti-guided cores within the ribbon. Our modeling predicts this design will scale to 100 embedded gain cores with reasonable tolerance limits on material construction and ribbon fabrication processes. A second drawback to achieving high average power fiber lasers is the need to deliver the pump light into the end of the fiber requiring diodes with radiance-conditioned outputs. Our design benefits from the planar ribbon structure, allowing it to conceivably be pumped from the side by diodes without radiance conditioning. This pumping concept will not be described in this paper, however. Additionally, the use of the ribbon structure is advantageous from a thermal management perspective and should allow all gain cores to be held at the same temperature.

The most commonly used approach for phase locking multiple apertures or gain cores is to evanescently couple cores to their nearest neighbors. This technique, originally used with multi-stripe diode lasers,[6] has been described in numerous papers.[7, 8] However, with evanescent phase locking the supermode or eigenmode tends to be

localized on gain cores and only nearest neighbors communicate with one another. When coupling many cores evanescently, it is anticipated that a general degradation of the phase fidelity for cores will occur the farther away from each other they are. Additionally, there are diffractive coupling techniques such as the Talbot plane methods[9,10] and the more recent 1-to-N-way phase-locking techniques[11,12]. The ribbon structure described in this paper uses a non-evanescent approach to coherently phase together multiple gain-loaded cores. In this approach, the gain elements are radiatively coupled in a "leaky" waveguide array, analogous to the most successful scheme for phasing laser diode elements.[13,14] Because the eigenmode is delocalized across all gain cores in this case, all gain cores communicate with all other gain cores. The antiguided cores are arranged in a row in a long aspect ratio rectangle or "ribbon" with a slightly higher index than the outer pump-cladding medium. An example structure with five cores is shown schematically in Fig. 1. The strong phase locking inherent in this approach should allow all the gain cores in the ribbon to communicate with each other and therefore scale to higher powers with higher phase fidelity across the aperture, compared to similar evanescently coupled structures.

Because of the ribbon-like structure, a one-dimensional transverse treatment provides a reasonable model for the properties of these devices. This paper describes a simple, but elegant, technique using electric field propagators to generate the eigenmode spectrum of the structure. A full two-dimensional transverse analysis follows to accurately assess modal gain discrimination. The modeling shows some striking results in the eigenmode spectrum. Maximum mode discrimination occurs with $n = 0$ (constant index) in the ribbon part of the structure, giving the best potential design for a high average power, single mode laser. However, when the index is allowed to vary slightly between the gain and non-gain regions the spectrum shows formation of "forbidden" regions of wavevector values. This is similar to the effect seen in "holey" fibers—photonic crystal fibers constructed with physical holes in the glass.[15] The holes serve to provide a periodic modulation in the refractive index, something our design does by using materials with different refractive indices. The width of the bandgap can be adjusted by varying the index difference between the gain and non-gain regions providing an ability to "tune" the structure to best suit an application requiring bandgaps.

To explore key aspects of our proposed ribbon fiber, we start by investigating a 5-core device in both the one-dimensional and then the two-dimensional analysis.
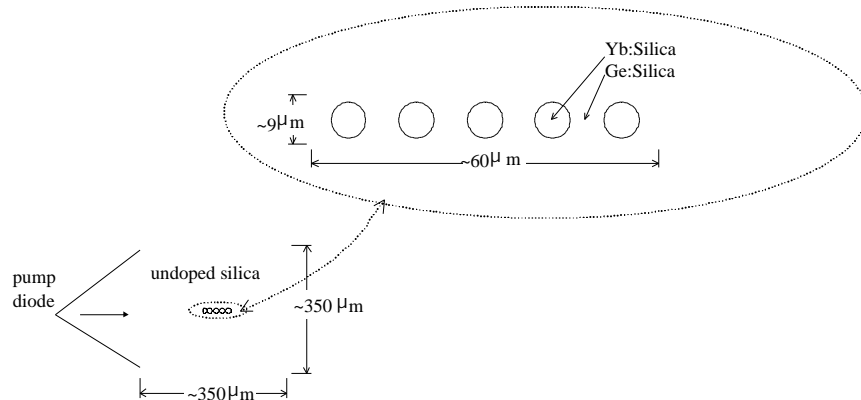

Figure 1 Cross-sectional view of 5-core ribbon fiber.

As a specific example, the structure shown in Fig. 1 could be fabricated out of pure fused silica along with germanium and fluorine dopants to control the refractive index, and Yb or Nd doping to provide the gain-loaded regions. In the structure shown in Fig. 1 the round doped core sections serve as the gain regions for the optical wave that is confined to the ~9 Οm high by ~ 60 Οm wide rectangular waveguide region. The pump radiation is confined to the larger ~ 350 Οm by ~ 350 Οm square region, which we here assume is pure silica and so has a lower refractive index than the waveguide region.

As already mentioned there are two critical design considerations for the structures we will consider here: first they must strongly favor oscillation in a single transverse mode; and second, the strongly favored mode must exhibit good intensity uniformity across the entire array of gain cores. We require single mode operation so that a static phase corrector placed in the near field of the ribbon laser's output can optimize the phase across the aperture to achieve a high Strehl ratio output beam. The second requirement that the strongly favored mode exhibit good uniformity across the entire array of gain cores is necessary to ensure that the ribbon structure's gain saturates in a uniform manner, so as not to increase the propensity of the device to operate in multiple transverse modes.

2. Theory of One-Dimensional Ribbon Fiber with Gain and Refractive Index Variation

To motivate our results, we begin by analyzing the simpler problem of the one-dimensional structure that is related to the two-dimensional structure of Fig. 1. We take a lineout of the index profile along the centerline of the Fig. 1 structure, and plot in Fig. 2 a particular refractive index profile to serve as an illustrative case. To further simplify our analysis we will also assume the electric field polarization corresponds to a TE wave.
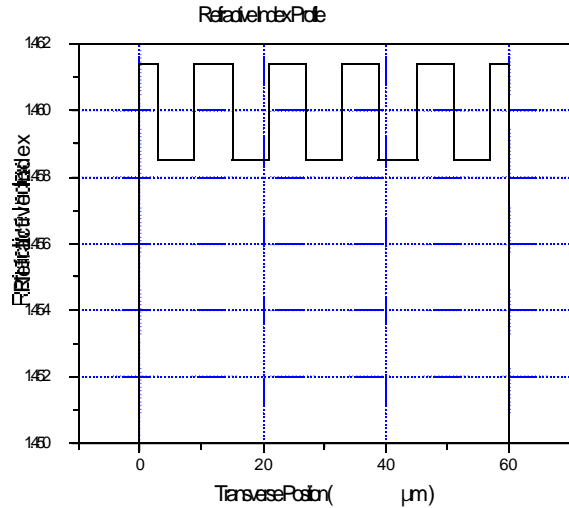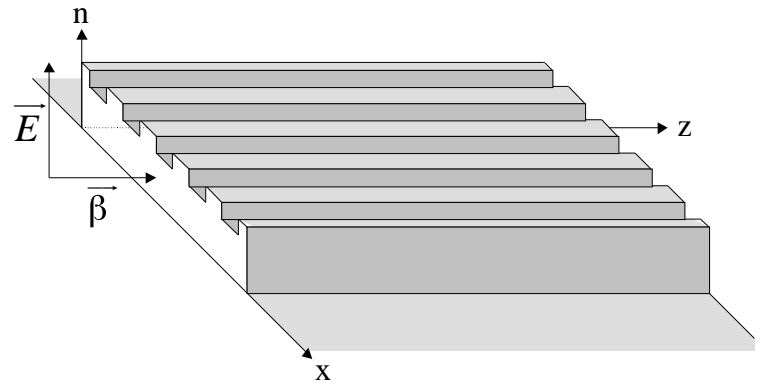
(a)   (b)

Figure 2 (a) Refractive index profile as a function of transverse position in the one-dimensional approximation to the ribbon waveguide structure shown in Fig. 1. The gain regions coincide with the lower index segments in the waveguide region. (b) Coordinate system used in our analysis for the TE polarized wave (TE w.r.t. refractive index boundaries) as shown, the E-vector is assumed to point in the y-direction. Assuming fused silica is the base optical material, the pump cladding index is 1.45, the gain regions have index 1.4585, and the no-gain regions within the waveguide have index 1.4614. The central segments within the waveguide are each 6 μm wide and the end segments within the waveguide are 3 μm wide.

We begin with the wave equation for the electric field in one of the constant index strips along the waveguide,

$$\tag{1}$$

Restricting the electric field to be TE polarized (the electric field parallel to the interfaces between the index segments that make up the ribbon), we write the electric field in terms of its frequency, ◆, and longitudinal k-vector, $\delta\ell$, as,

$$\tag{2}$$

where   is a unit vector in the y-direction. Substituting (2) into (1), then gives the equation that must be satisfied by E(x),

$$\tag{3}$$

which is the one-dimensional Helmholtz equation,[16] or an eigenvalue equation for the Laplacian. Due to the polarization direction of the electric field (TE wave), the boundary condition to be satisfied at the interfaces between neighboring strips having differing refractive indices in Fig. 2 is one of continuity, i.e., the electric field amplitudes are the same on each side of the boundary. In addition to the continuity of the electric field amplitude at the interfaces in the ribbon structure, the second order differential equation (3) for the electric field amplitude imposes a continuity condition on dE/dx at the interfaces. If dE/dx where not continuous at the interfaces, then d^2E/dx^2 would blow up at those locations leading to infinitely large values of the electric field. Finally, the boundary condition on the electric field amplitude outside of the rectangular waveguiding structure of Fig. 2 is that it approaches zero at large distances from the waveguide. Summarizing, the boundary conditions to be satisfied by the electric field are,

$$\tag{4}$$

$$\tag{5}$$

$$\tag{6}$$

where x_i^- and x_i^+ refer to the limiting values of x at the ith interface when approached from the negative and positive sides, respectively. Because we are specifically interested in ensuring we develop designs that will preferentially support only a single transverse

mode, we must find all electric field eigenmode solutions to (3) that satisfy the boundary conditions (4) through (6). These eigenmode solutions will be defined in terms of their longitudinal k-vector values, β.

Several methods of solution are available for generating solutions to the one-dimensional problem outlined above, for example the transfer, or T-Matrix method.[17] Our method of solution, as outlined here, will be to arbitrarily define an electric field amplitude of unit intensity at x=0 for the structure in Fig. 2, and then assume a k-vector value. To determine whether the assumed k-vector value corresponds to an actual eigenmode of the structure, we will then propagate the electric field across the structure from x=0 to well beyond the waveguiding portion of the structure (past 60 μm in Fig. 2). Applying boundary condition (6) then demands that if the assumed k-vector value corresponds to an actual eigenmode, the electric field amplitude will approach 0 as x increases without bound.

The propagation of the electric field across the structure can be carried out numerically using (3) to incrementally step E and dE/dx across the structure given initial values for both quantities at x=0. However, a quicker method and the one we use here takes advantage of analytic propagators to propagate the field across an entire constant index segment of the structure in a single step. The advantage of the analytic propagator method, which we outline below, is that it is extremely efficient and applicable to very large structures (hundreds of cores) that would bog down the calculation using the more straightforward numerical incremental step calculation.

To begin the calculation, we arbitrarily choose a target k-vector value for β in (3) and define both E and dE/dx at x=0⁻ in Fig. 2. Since we require E(x) approach 0 as x approaches -∞ we must choose $\beta > n_{clad}\omega/c$, where n_{clad} is the refractive index value in the cladding region x<0 or x>60 μm in Fig. 2. As already mentioned, we can arbitrarily set the value of E(x=0⁻)=1, however the value of dE/dx|$_{x=0}$⁻ is not arbitrary. The functional form of E(x) for x<0 is

$$
\sqrt{\quad} \qquad , \tag{7}
$$

which decays exponentially to 0 as x→-∞. With E(x) given by (7), the value of dE/dx|$_{x=0}$⁻ is given by,

$$
\quad \sqrt{\quad} \quad . \tag{8}
$$

We denote the refractive index of the ith constant index segment of the waveguide structure described in Fig. 2 by n_i. Starting with the electric field amplitude and its first derivative at the left hand side of one of the constant index segments, the electric field amplitude and its derivative at the right hand side of the constant index segment is given by,

$$\kappa_i \quad \underline{\qquad} \tag{9}$$

or

$$\kappa_i \quad \underline{\qquad} \tag{10}$$

where l_i is the width of the ith constant index segment in the ribbon fiber structure. The character of the electric field solution in any given index segment is strongly dependent on the relationship between the value of $\delta\Omega$ and $n_i \bullet /c$. In the case of $\delta\Omega < n_i \bullet /c$, the solution is delocalized and the field propagates across the waveguide segment with an oscillatory behavior but does not decay in amplitude. In the case of $\delta\Omega > n_i \bullet /c$, the solutions are localized and the fields have an exponential dependence on the transverse coordinate in the waveguide segments, which is the situation one normally thinks of as evanescent coupling. In our analysis we are primarily interested in the delocalized solutions ($\delta\Omega < n_i \bullet /c$) in which every gain regions is coupled to every other gain region

Using the transverse propagator method outlined above, trial values of the wave vector $\delta\Omega$ in (2) can be propagated across the waveguide structure. The requirement that the trial $\delta\Omega$ value correspond to an actual electric field eigenmode of the structure is that as $x \ast \odot$ on the right hand side of the waveguide, the electric field amplitude goes to zero. In general, a trial value for $\delta\Omega$ will generate an electric field amplitude that either diverges toward $+\odot$ or $-\odot$ as $x \ast \odot$. This suggests a general method to search for electric field eigenmode $\delta\Omega$ values. If two nearby $\delta\Omega$ values can be found that generate fields that diverge in opposite directions as $x \ast \odot$, then by continuity there must be an intermediate $\delta\Omega$ value such that the field it generates goes asymptotically to 0 as $x \ast \odot$, i.e., a $\delta\Omega$ value corresponding to an actual electric field eigenmode. An example of this method is illustrated by the field calculations displayed in Fig. 3.

Electric Field and Refractive Index Profiles

4

3

1466

1464

diverges to $+\odot$

eigenmode

Field

Rel
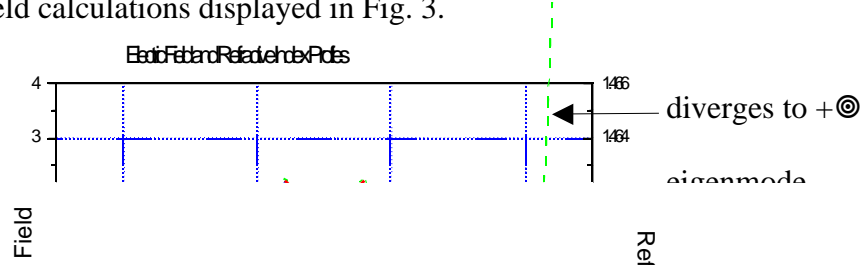
The $\delta\Omega$ values used for the calculations in Fig. 3 are as follows:

$\delta\Omega$=8.7167195x(0.99999), field diverges to -
$\delta\Omega$=8.7167195, field converges to 0
$\delta\Omega$=8.7167195x(1.00001), field diverges to +

This technique is generally applicable to arbitrary waveguide structures and can quickly yield the entire spectrum of a given structure's allowed eigenvalues and eigenmodes.

The gain experienced by different laser modes is proportional to the overlap, Γ, of the mode's intensity envelope with the gain-loaded portion of the fiber,

$$\frac{\int g(x)\,|\quad|}{|\quad|}, \tag{11}$$

where g(x) is a function with value unity in those portions of the fiber that are gain loaded and 0 where there is no gain loading. This is a straightforward calculation once the eigenmode fields are known. Additionally, the effective index values, n_{eff}, associated with the various eigenmodes of the structure can be calculated using,

$$\frac{\quad}{\quad}. \tag{12}$$

From (12) it is seen that c/n_{eff} is just the phase velocity associated with the eigenmode as it propagates in the ribbon structure. Using (11) and (12), the electric field that propagates down a gain loaded ribbon fiber structure can be written as,

$$\tag{13}$$

where $\boxtimes$ is the gain per unit length in the gain-loaded portion of the ribbon fiber structure. Rewriting (13) and introducing the effective index defined in (12), but extending it to complex values gives,

$$\tag{14}$$

With this expression, one immediately sees the connection between ϕ and the imaginary part of the complex effective refractive index,

$$\tag{15}$$

3. Design Criteria for a Single Intensity Lobe in Each Gain Core

Here we deduce the design rules for the one-dimensional ribbon structure that supports a mode having a single intensity lobe in each of its gain cores and constant peak intensity from gain core to gain core. Additionally, we require this mode to have the highest gain overlap of all the modes supported by the structure to ensure it is the lowest threshold of all the modes supported and thereby lases preferentially over the other modes. Equation (3) hints at how to proceed. If we can arrange for the electric field to null at the center of the undoped no-gain segments that separate the doped gain segments within the waveguide region, then the lobes of the intensity envelope will center themselves on the gain regions and ensure a high overlap mode. To proceed we will fix a wavevector value for this preferred mode and then construct the ribbon structure by varying the widths of the gain and no-gain regions until the above-described conditions pertain. Calling the refractive index values of the gain and no-gain regions n_g and n_{ng} respectively, we adjust the widths of the gain and no-gain regions such that the following equation is satisfied,

$$\sqrt{} \qquad \sqrt{} \qquad ,\tag{16}$$

where l_g and l_{ng} are the widths of the gain and no-gain segments, respectively. Equation (16) ensures one complete lobe will be associated with each gain segment that makes up

the ribbon structure. Having ensured that only one lobe of the intensity envelope will be associated with each gain segment in the ribbon structure, the remaining issue concerns the design of the end segments of the ribbon structure to ensure the intensity lobes are centered on the gain segments. Since the boundary conditions for the outer segments (the segments at the extreme ends of the waveguide structure) are different than that of the interior segments due to the difference in the index steps there, separate consideration must be given to their widths beyond the constraint given by (16). For definiteness, we will assume the outer segments are gain-loaded in our structure. With this constraint, we can then ensure an intensity lobe will be centered on the first gain-loaded segment at the boundary by forcing the field to null in the center of the first no-gain segment, which is next to the boundary gain-loaded segment. To generate an equation representing this constraint, we use the boundary condition (8) and the field propagators given in (9) to first propagate the field from the left-hand boundary of the waveguide region through the first gain-loaded segment and then to the midpoint of the first no-gain segment where we force the field to null. After some algebraic manipulations, the resultant equation representing this constraint is,

$$\text{(17)}$$

where n_{clad} is the index of the pump cladding surrounding the waveguide region and l_{edge} is the width of the gain-loaded edge region. To illustrate in detail the above described procedure we investigate the ribbon structure defined in Table I below with 5 gain-loaded cores.

Table I Detailed Design of One-Dimensional Ribbon Fiber Structure with Step Index
Between Gain and No-Gain Segments

width (microns)	refractive index	gain loaded?
10.00	1.45	no
11.23	1.4585	yes
4.00	1.4614	no
4.00	1.4585	yes
4.00	1.4614	no
4.00	1.4585	yes
4.00	1.4614	no
4.00	1.4585	yes
4.00	1.4614	no
11.23	1.4585	yes
10.00	1.45	no

In this structure, the pump-cladding index region has refractive index 1.45, the gain-loaded portion of the waveguide has refractive index 1.4585, and the no-gain regions of the waveguide have refractive index 1.4614. We arbitrarily take the vacuum wavelength of the waveguide radiation to be 1.05 μm and the widths of the interior gain and no-gain segments to be 4 μm. With these choices, the mode having one lobe associated with each gain region has a wavevector value of 8.725/μm and the gain-loaded segments at the ends of the waveguide region have widths of 11.23 μm as determined from (17) making the total width of the waveguide region 50.45 μm. Figure 4 gives a summary of this structure's eigenmode spectrum in a plot of mode overlap with gain regions vs effective index value.
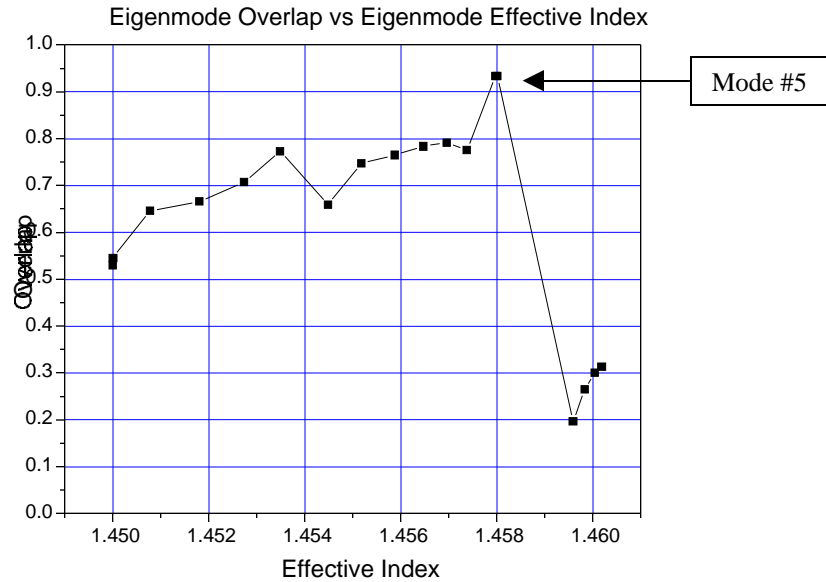

Figure 4 The eigenmode overlap with the gain region is plotted against effective index. Mode #5 (counting from the right) was designed to have a single intensity lobe for each of the gain-loaded segments in the waveguide region.

Figure 5 shows a plot of local mode intensity across the waveguide structure for the mode for which the waveguide structure was designed.
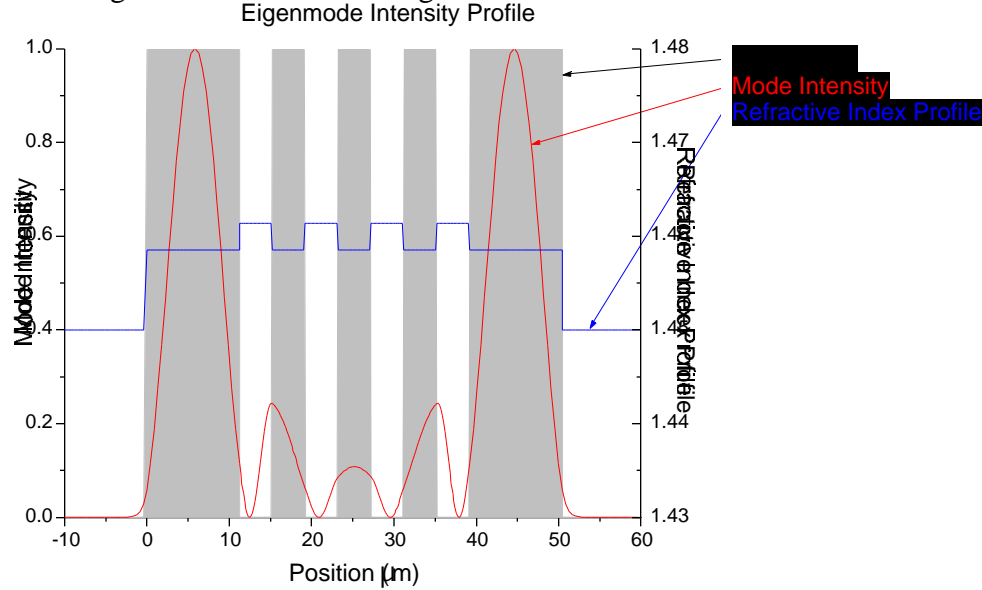

Figure 5 Intensity envelope of the eigenmode for which the ribbon structure was designed (mode #5 in Fig. 4). The widths of the individual index segments are adjusted so that each gain region (indicated in gray) sees a single intensity lobe. Superimposed is the refractive index profile of the structure. The gain is located in the lower index regions within the waveguide structure.

The ribbon structure having the mode spectrum plotted in Fig. 4 was specifically designed to ensure a mode would exist having wavevector 8.725/⊙m (the mode plotted in Fig. 5), and that this mode would have a single intensity lobe in each of the gain-loaded segments of the waveguide. Having a single intensity lobe in each of the gain-loaded regions of the structure ensures this mode has the highest gain overlap of all the modes supported by the structure.

Although the mode shown in Fig. 5 has the highest gain of all the modes supported by the structure, it does not have constant lobe intensity in the gain regions across the ribbon structure. The two outlying gain regions see almost 10 times the peak intensity of the central gain region. Under conditions of strong gain saturation that would be required for efficient laser performance, this implies the outlying regions will be more strongly extracted than the central regions, leaving an unbalanced gain profile across the structure. This in turn may encourage additional modes coming in that preferentially extract the central gain regions. Specifically designing the ribbon structure to ensure the peak intensity is unchanged from core to core is addressed in the following section.

4. One-Dimensional Structures with Gain Variations and Constant Refractive Index

As an alternative to the periodically modulated index structures just considered, we now evaluate a waveguide structure having uniform refractive index across its aperture and only modulate the gain profile periodically. To keep a connection with the

previously analyzed case displayed in Fig. 4, we keep the outer clad index value at 1.45, the waveguide region at a constant index of 1.4585, and the overall width of the waveguide at 50.45 ⌀m. Applying the same design procedure as just used for the case in which the gain segments had slighltly lower refractive index than the no-gain segments, the generated 5-core ribbon structure in this case is as summarized in Table II .

Table II Detailed Design of One-Dimensional Ribbon Fiber Structure with Constant Index Waveguide Region

width (microns)	refractive index	gain loaded?
10.00	1.45	no
6.81	1.4585	yes
5.26	1.4585	no
5.26	1.4585	yes
5.26	1.4585	no
5.26	1.4585	yes
5.26	1.4585	no
5.26	1.4585	yes
5.26	1.4585	no
6.81	1.4585	yes
10.00	1.45	no

For the structure detailed in Table II, the mode having one lobe associated with each gain region has a wavevector value of 8.723/⌀m. Figure 6 gives a summary of this structure's eigenmode spectrum in a plot of mode overlap with gain regions vs effective index value.
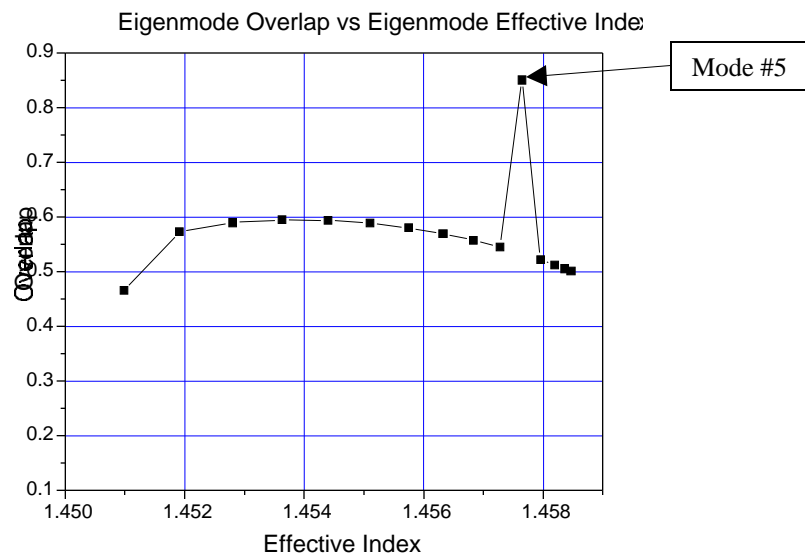

Figure 6 The eigenmode overlap with the gain region is plotted against effective index. Mode #5 (counting from the right) was designed to have a single intensity lobe for each of the gain-loaded segments in the waveguide region.

Comparing Fig. 6 to Fig. 4, it is seen that one of the advantages of the constant refractive index waveguide region is that the mode discrimination between the desired mode and all other modes supported by the structure is much better than for the varying index waveguide region (Fig. 4). Figure 7 shows a plot of local mode intensity across the waveguide structure for the mode for which the waveguide structure was designed (mode #5 in Fig. 6).
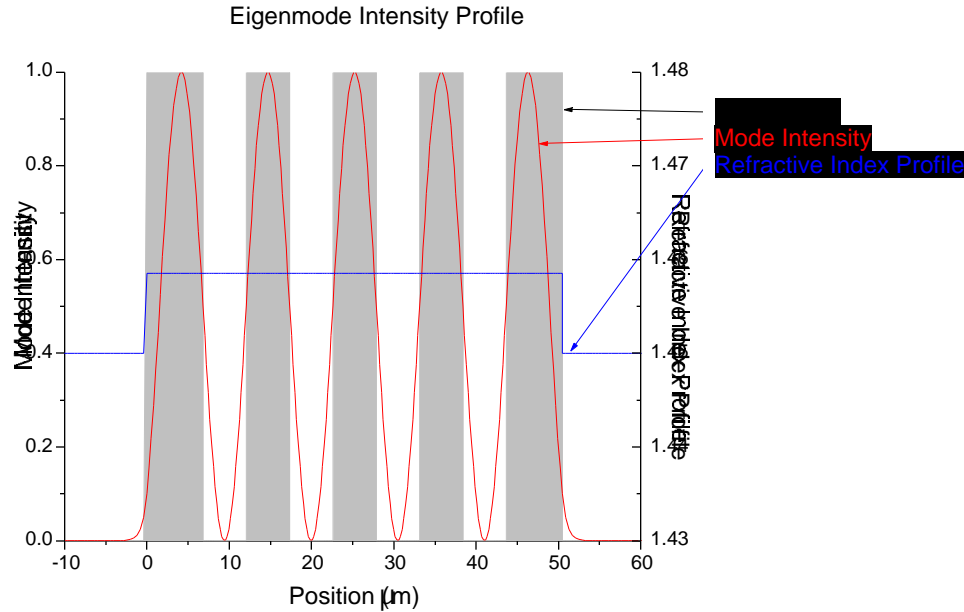

Eigenmode Intensity Profile

Figure 7 Intensity envelope of the eigenmode for which the ribbon structure was designed (mode #5 in Fig. 6). The widths of the individual index segments are adjusted so that each gain region (indicated in gray) sees a single intensity lobe. Superimposed is the refractive index profile of the structure, which is constant across the waveguide region.

Examining the mode structure in Fig. 7, it is seen that the peak lobe intensity is constant across the waveguide structure, which as already discussed is one of the goals of a robust design. This combined with the enhanced mode discrimination afforded by the constant index waveguide region over other structures having varying index in the waveguide region, makes the constant index structure ideal for single mode, power scalable devices. The realization of these advantages brought on by having a constant index waveguide region is the central result of this work. It should be noted that the gain discrimination depicted in Fig. 6, which clearly favors the single mode plotted in Fig. 7 (mode #5), is calculated for the specific case in which the gain in the interior regions has a 50% fill factor, i.e., the interior gain and no-gain regions have the same width. By increasing the fill factor of the gain regions beyond the 50% fill design point considered above, the Γ factor of the preferred mode can be increased beyond its value of 0.85 in Fig. 6. This however will come at the expense of mode discrimination, as the Γ factor of all other modes will also increase.

5. One-Dimensional Structure with Gain and Index Variation

Figures 8 and 9 reveal the impact of slightly increasing and decreasing, respectively, the refractive index of the gain-loaded segments by n=0.001. By comparing these calculations of the overlap factor versus the effective index with the prior calculation of Fig. 6, it becomes apparent that a "bandgap" emerges when n 0. As will be illustrated, the refractive index plays the role of a potential, when an analogy is drawn between the paraxial wave equation of optics and the Schroedinger equation of quantum mechanics (see Section 6). Therefore, we are able to say that each segment in the ribbon may be viewed as an "atom".

For the case of Fig. 8, where n (gain – no-gain) = +0.001, it is as if a potential well has been introduced in the gain-loaded regions. This favors the overlap factors of the modes having five or less lobes, (i.e. the first five points, counted from the right of Fig. 8). The sixth point (six lobes) fills the no-gain regions much more effectively, introducing a discontinuity in the vs. n_{eff} plot. Once there are many lobes in the mode, the overlap averages to approximately one-half, as would be expected. The point of highest overlap may be regarded as the top of the valence band (maximal overlap with the gain-loaded segments), while the point characterized by the lowest overlap factor (i.e. maximal overlap with the no-gain regions), may be regarded as the bottom of the conduction band. We thereby discern the "photonic crystal" nature of the Ribbon Laser.[18, 19, 20] The calculations in Fig. 9 are related, but may be contrasted since the potential well (i.e. slightly higher index) is located in the no-gain segments. Therefore the field becomes concentrated in the no-gain regions and evidences a very low overlap factor for the case of less than 4 lobes. The discontinuity here may also be interpreted as a photonic bandgap.

We may now refer back to Figs. 6 and 7, where mode #5 exhibits a greatly enhanced overlap factor compared to all the other modes. The reader is reminded that this case corresponds to a constant refractive index across the ribbon. Upon considering the solid state analogies again, it is apparent that the constant-index, or constant potential scenario, is closest to that of a nearly-free electron in a metal. Of course, a *photonic metal* would not have a bandgap, but the special mode (#5) would correspond to the boundary of the Brillouin Zone. This analog of a photonic metal holds most closely for the situation where the electron is nearly-free (i.e. does not sense the potential from individual atoms in the lattice).
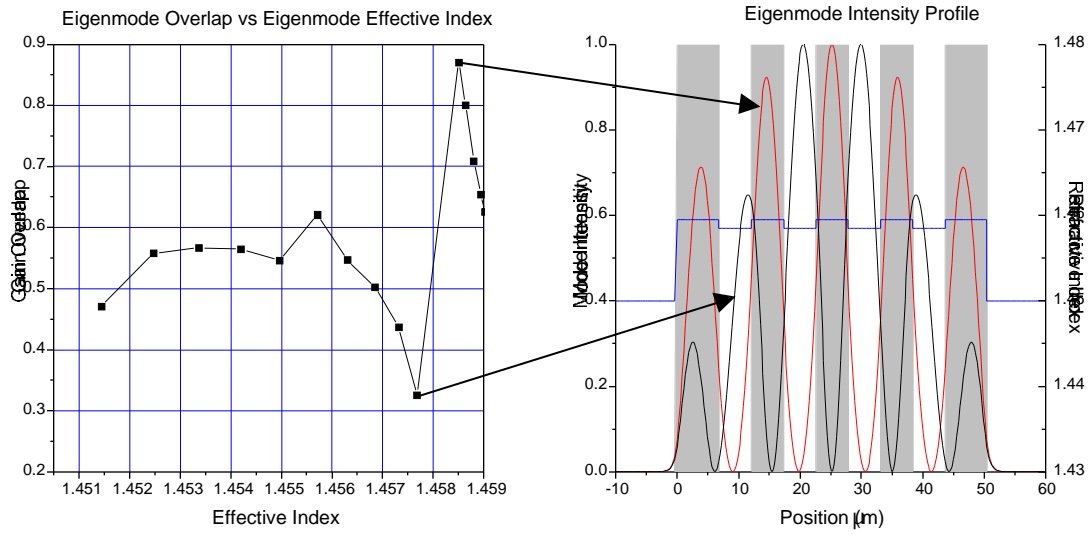
Figure 8 The same structure as shown in Fig. 7 but with the gain-loaded segments refractive index increased by 0.001 above that of the no-gain segments. Gain-loaded regions are indicated by gray.
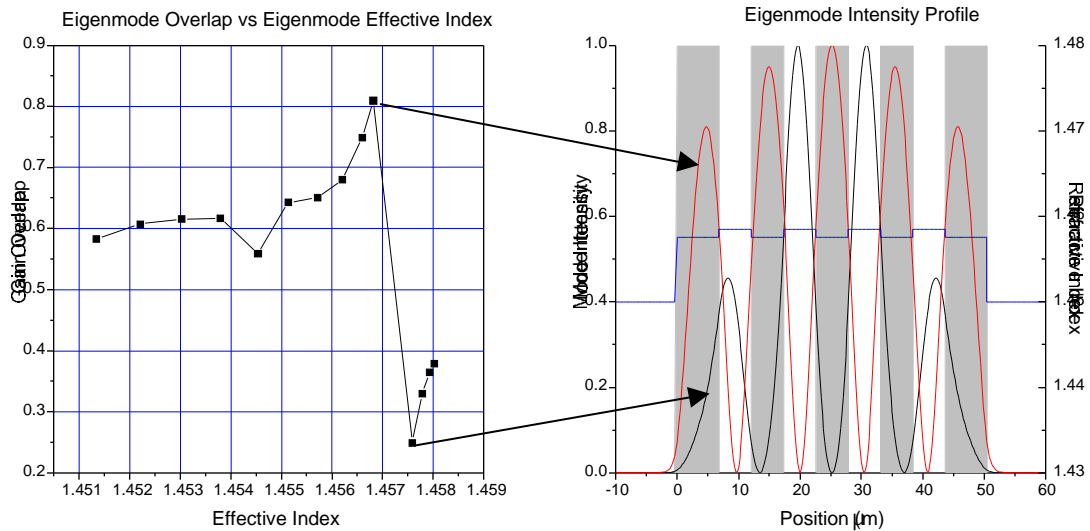

Figure 9 The same structure as shown in Fig. 7 but with the gain-loaded segments refractive index decreased by 0.001 below that of the no-gain segments. Gain-loaded regions are indicated by gray.

6. Theory of Two-Dimensional Ribbon Fiber

The one-dimensional theoretical model outlined above gives insight into the occurrence of desired anti-guided leaky modes in structures of the type considered here. In order to understand effects on performance of possible fabrication constraints, we have considered a number of designs with either rectangular or circular cores that either touch the boundary or are immersed in the inner cladding region. For this reason, we have employed a full scalar-wave propagation method to simulate the performance of target designs as detailed below. Various implementations correspond to the same one-dimensional transverse structure (index distribution as seen on center line) analyzed in the preceding section.

The amplitude ε of a propagating electric field in normal fiber and integrated optical waveguides with small index contrast, i.e. where refractive index differences are small compared to the index, is well described by the scalar Helmholtz wave equation.[21]

$$\overline{\qquad}\tag{18}$$

Here n(x,y) is the refractive index which is assumed to depend on the transverse spatial coordinates x and y. Because the index is independent of z (position along the ribbon fiber), such a structure supports modes whose shape is independent of z. Such a mode $E_i(x,y)$ propagates with a characteristic propagation constant $_i$ which can be found from the eigenvalue equation,

$$\overline{\qquad}\ ,\tag{19}$$

here $\overline{\qquad}\ \overline{\qquad}$ is the transverse Laplacian operator. Equation (19) is equivalent to (3) but incorpoarates both tranverse dimensions. Since (18) is linear, the general solution is a linear combination of such modes with arbitrary amplitudes, each changing its phase with propagation distance according to its own characteristic modal propagation constant.

Numerical solution of (18) can be difficult. However, a convenient simplification is to make the slowly varying envelope approximation. We assume that the amplitude *u* varies mainly as exp(iK$_c$z) where K$_c$ is a reference wavenumber (see below), i.e. we let

$$\ ,\tag{20}$$

where E is only a very weak function of z. This means E varies little over an optical wavelength. In this case, substituting (20) into (18) and discarding the term $^2E/\ z^2$ since it is small compared to $K_c\ E/\ z$, we are left with the so-called paraxial wave equation

$$\overline{\qquad}\ \overline{\qquad}\ \overline{\qquad}\ \overline{\qquad}\tag{21}$$

where n_c is the index corresponding to K_c, i.e. $K_c = n_c$ /c. Note that this equation has exactly the form of the Schroedinger equation of quantum mechanics. Propagation distance z plays the same role in optical propagation as time does in the Schroedinger equation and the "potential energy" is given by the second right hand side term in (21) involving the refractive index. There is thus a one to one analogy between optical waveguides and 2-dimensional (x,y) quantum mechanics. Equation (21) defines an optical Hamiltonian operator H as in quantum mechanics. The eigenvalues and eigenfunctions of this operator are the fundamental quantities that describe the nature of the optical waveguide.   It can be shown that the modal eigenfunctions of Eqs. (19) and (21) are exactly the same.[22] However, their eigenvalues are different. The modes that comprise the field E of (21) individually satisfy the eigenvalue equation,

$$ \qquad (22) $$

with the relationship between $_i$ and $_i$' given by,

$$ \sqrt{\qquad} \qquad . \qquad (23) $$

That is, '$_i$ represents the small change of the modal wavenumber   from the reference wavenumber K_c. Because of the analogy with the Schroedinger equation, we see immediately that if we choose the cladding index to define K_c, then guided modes will have negative values of '$_i$ (corresponding to bound states in quantum mechanics having negative energy) and radiation modes will have positive values of   '.

        We solve (22) numerically using the Fast Fourier Transform based Beam Propagation Method (BPM).[23, 24] An advantage of this approach is that for a lossless/gainless medium, it exactly conserves electromagnetic energy. This is important so that reliable calculations can be carried out for a medium with small gain or loss. The solution found for (21) is of the form E(x,y,z) where E is, in general, a linear combination of modes excited at the start of the calculation by assumption of an initial field E(x,y,0). The modal propagation constants can be found by forming a correlation function P(z)

$$ \qquad . \qquad (24) $$

Since E is a linear combination of orthonormal modes, the correlation will necessarily be of the form

$$ \qquad \left| \; \right| \qquad . \qquad (25) $$

Where A_n is the amplitude of mode n and $|A_n|^2$ is proportional to the power in mode n. Fourier transforming P(z) with respect to z yields

$$\tilde{K} \qquad \qquad \left| \quad \right| \qquad \qquad . \tag{26}$$

That is, the spectrum of the correlation function consists of distinct lines centered at the modal propagation constants. Once the modal propagation constants are known, the unnormalized mode shapes can be retrieved by projecting them from the propagated field, i.e.,

$$\tilde{\kappa}_{(x,y)} \qquad \qquad . \tag{27}$$

This technique has been used very effectively in modeling optical fibers, rib waveguides, x and y couplers and optical resonators.[25]

  The above formalism remains the same in the case of a non-passive device, i.e. a device with distributed gain or loss. In this case, the delta function lineshapes in the spectrum of (26) are broadened by an amount proportional to the imaginary part of the modal wavenumber. A numerical technique that "measures" this width, then gives a direct value for the modal gain.

7. Two-Dimensional Structure with Gain Variation and Constant Refractive Index

We have used a numerical code embodying the above formalism in our simulations of the 2-dimensional transverse ribbon structure. Typically, the inserted field is propagated on a 256x64 grid and the propagated field evaluated as a function of transverse coordinates x and y at 32800 longitudinal z values. The complex modal propagation constants and modal field patterns can then be calculated. A cross section of a sample ribbon laser structure is shown in Fig. 10. Both refractive index and small signal gain are spatially distributed. Simulations are started with an initial field. Part of this field projects onto waveguide modes and is propagated. The rest is radiated away from the structure. To prevent this radiated energy from reflecting from the numerical boundaries of the simulation, an absorbing layer is placed around the outer boundary.
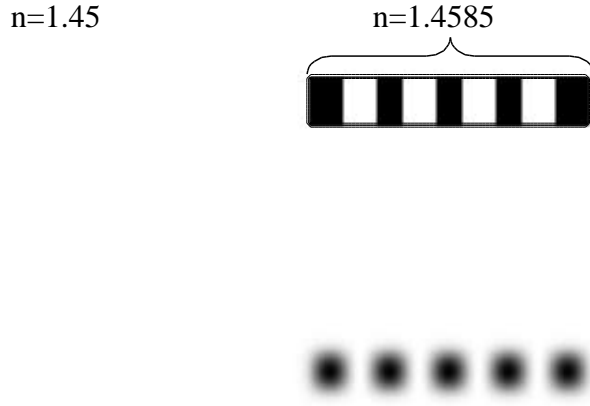
Figure 10 Cross sectional view of ribbon structure with 2 transverse dimensions that is analyzed in the text. The dark regions in the upper picture indicate the gain-loaded portions of the waveguide. The refractive index is constant throughout the waveguide region and equals 1.4585. The waveguide region is 6 μm high, the end pieces are 4.5 μm wide, and the central segments are 4 μm wide.

Propagating the initial field and calculating the correlation function defined in (25) and its Fourier transform over the propagation distance leads to the spectrum shown in Fig.11. Excited modes appear as distinct spectral lines for which the spectral width is proportional to the modal gain.   Figure 12 plots the gain overlap vs effective mode index for the strucuture shown in Fig. 10 using both the 1-D and 2-D formalism. The 1-D calculation corresponds to the one-dimensional structure generated by by taking a line out along the x-axis of the two-dimensional structure depicted in Fig 10.
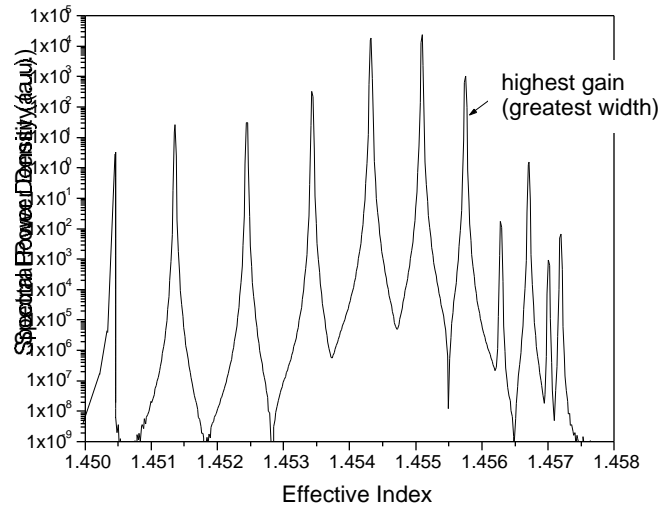

Figure 11 Spectral power of modes excited by Gaussian beam inserted into structure described in Fig. 10.
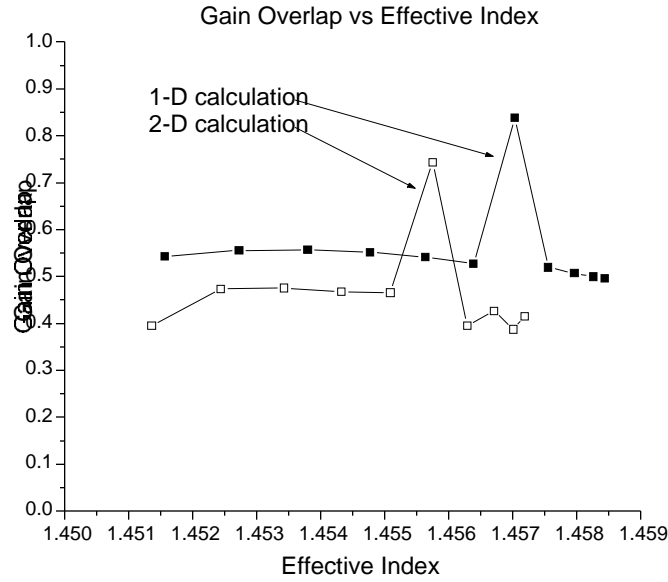
Gain Overlap vs Effective Index

1-D calculation
2-D calculation

Gain Overlap

Effective Index

1.0
0.9
0.8
0.7
0.6
0.5
0.4
0.3
0.2
0.1
0.0

1.450 1.451 1.452 1.453 1.454 1.455 1.456 1.457 1.458 1.459

Figure 12 Comparison of gain overlap vs effective mode index for 1-D and 2-D calculations.

In both the 1-D and 2-D analyses, the 5th mode is the one with the highest gain. As one would expect, the 2-D calculation gives both smaller gain overlaps and smaller effective index values because of the extra degree of freedom in the transverse direction.

As can be seen, e.g. in Fig.(7), the optimal anti-guided modal field is very nearly a pure sinusoid. This implies the farfield will principally consist of two lines with an angular spread of $\pm$ /np in the horizontal direction. Here /n is the wavelength in the medium and p is the period. Similarly, the angular spread in the vertical direction is determined by the structure height. These expectations are met in our numerical simulations. Figure 13(a) shows the simulated farfield pattern for the ribbon structure of Fig.(10).   Because the modal field is coherent, collimation can be achieved by use of a phase plate. Additionally, since the modal structure is so simple, the most convenient approach is to adjust the phase of periods of the structure by either 0 or , successively, to effectively yeild the absolute value of the modal field. This elimination of zero crossings greatly improves the farfield pattern as shown in Fig. 13(b) where the simulation reveals that 2/3 of the modal power has been concentrated in a central peak. The horizontal width of this peak depends on the number of cells in the structure and will improve as 1/N for the ideal structure.
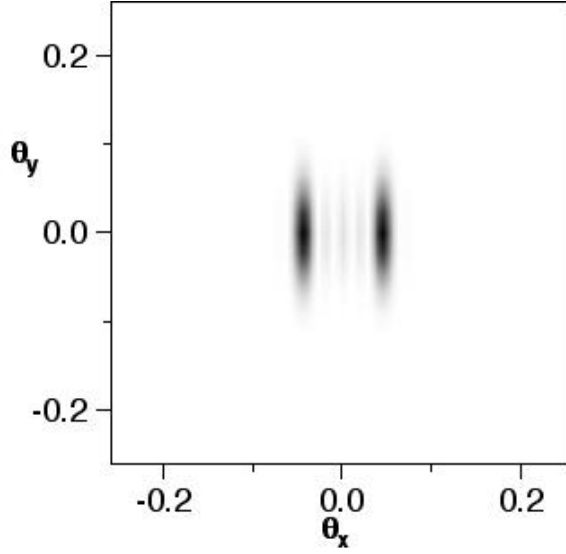
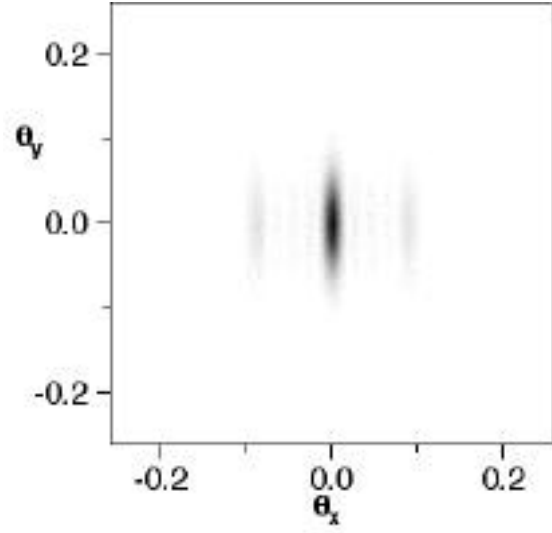*Figure 13(a): Uncorrected farfield of ribbon structure of Fig.(10). Farfield lines separated by 132 mrad.*

Figure 13(b) Farfield after correction with simple phase plate. Approximately 2/3 of the total energy is contained in the central peak.

8. Robustness to Variations in Refractive Index and Dimensions

The ultimate goal of this study is to develop an understanding of robust fiber ribbon designs that will guarantee single transverse mode operation in the presence of strong gain saturation. As such, it is useful to develop a criterion for how tightly design tolerances, both cell refractive indices and cell dimensions, must be held for the various cells that comprise a given structure. We investigate this issue in two different regimes. First we look at the impact of systematic variations in cell refractive indices and cell dimensions. This type of systematic error represents what we will likely see in structures fabricated using conventional fiber and preform pulling technology. Cell dimensions will tend to vary together, shrinking below or expanding above the design point due to the manner in which the ribbons are pulled. Also, because we anticipate using the same starting material for all the gain and all the no-gain portions of the various cells that comprise the waveguide region of the ribbon, we expect index errors from the desired design point to occur uniformly throughout the structure. In addition to investigating these systematic errors, we also then go on to investigate random errors in both cell refractive indices and cell dimensions for very large, 100 core structures. Such errors characterize uncontrolled aspects of the ribbon structure fabrication and could be an issue in the developing technology we anticipate using.

Here we determine what the tolerance in the refractive indices of the gain and no-gain regions must be to ensure the structure will support only a single transverse mode. Because the one-dimensional code can be quickly executed, it is better suited to running the large number of cases required for this parameter study. The two-dimensional code was then used on a smaller scale to confirm the results of the one-dimensional code. Using the same constant index 5-core structure as described in the previous section, a series of runs were made to determine sensitivity to systematic variations in the refractive indices of the gain and no-gain cells. In this series of runs, we kept the geometry

constant, allowing only the index difference to vary from run to run. We used an index of 1.45 for the cladding, while the gain-doped regions were held fixed at an index of 1.4585 and the non-gain regions were allowed to vary between 1.4628 and 1.4542. The data were compiled by the index difference value of "gain index – no-gain index". This range of allowed indices for the no-gain regions represents both "guided-like" (gain index > non-gain index) and "anti-guided-like" (gain index < non-gain index) variations.   For each index difference, the largest and second largest gain overlap modes were recorded. A total of 11 cases were run using the one-dimensional model. Five of the 11 cases were rerun using the two dimensional model. Figure 14 is a plot of Overlap vs. Index Difference and presents both the 1-D and 2-D results.
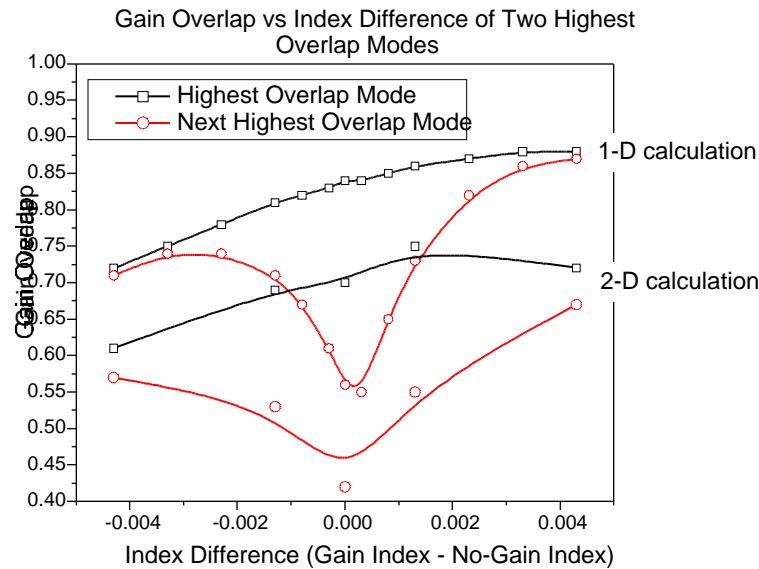

Figure 14 Overlap vs. Index Difference plot for 1-D and 2-D cases with systematic index variation between the gain and no-gain regions.

Although the gain-overlap increases as the index difference increases for the highest gain-overlap mode, Fig. 14 shows the point of maximum discrimination occurs with an index difference of zero.   In addition, evident in Fig. 14 is the qualitative similarity between the 1-D and 2-D calculations, both showing maximum gain discrimination for an index difference of zero. Remember, one of the critical design requirements is that the structure oscillates in a single transverse mode, making good mode discrimination a strong figure of merit in the design. As the index difference increases (in both the positive and negative direction), the overlap values of the two strongest modes get closer; increasing the chance the structure will "hop" from one mode to the other during operation.

We next explored the structure's sensitivity to geometry (cell width) variations. The dimensions of all cells within the structure were varied by the same amount, mimicking the type of systematic error that might be expected in fabricating the structure using a fiber preform pulling technique. For this parameter study we varied each cell

width by a specified amount (±2%, ±4%, ±6%, ±8%, and ±10%) from its original value. This parameter study was repeated for systematic index variations of -0.0013, 0.0, and 0.0013. All runs were done with the one-dimensional model. As seen in Figure 15 where the results of this study are plotted, varying the cell widths has little impact on either the gain overlap value or the mode discrimination out to the ⊕10 % systematic variations investigated here.
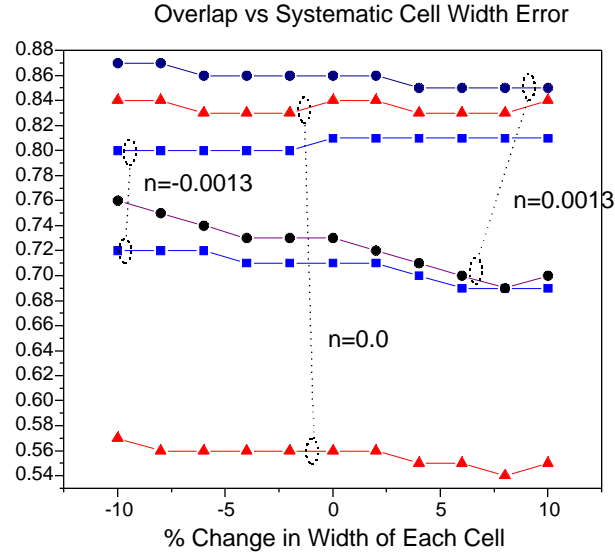

Figure 15 Gain Overlap vs. Index Difference of the two highest overlap modes for three different values of cell Δn. All data points were calculated using the one-dimensional model.

Based on these results, we feel an acceptable index difference is ±0.001 with a target difference of 0.0. Within this index difference range, we should be able to handle cell width fabrication errors of ±10% and possibly more.

Important for power scaling is the question of required index tolerance as a function of the number of cores. To answer this question, we have repeated the forgoing 5-core structure analysis in which the refractive index of the gain and no-gain cells was systematically varied for a 20 core and 100 core ribbon fiber structure. Figure 16 depicts the results of this study. The data in Fig. 16 was generated using the one-dimensional code with sub-cell dimensions identical to those used in Fig. 14. Evident in Fig. 16 is the observation that, as the number of cells increases the requirements on the systematic variation of the refractive index become more stringent. To better quantify this scaling law, we have determined the FWHM spread in index for which the gain discrimination between the two highest overlap modes just halves from its peak value at ◈n=0. These FWHM values are indicated in Fig. 16. In Fig. 17, we plot these FWHM index spreads against the inverse number of gain cores ($1/n_{cores}$) for the three cases studied here. As seen from the data plot in Fig. 17, the ◈n_{FWHM} requirement varies almost linearly with $1/n_{cores}$, which is what we intuitively expect. The straight line in Fig. 17 represents a linear least squares fit to the data points that is constrained to pass through the origin, ◈n_{FWHM} = 0.0127/ n_{cores}.
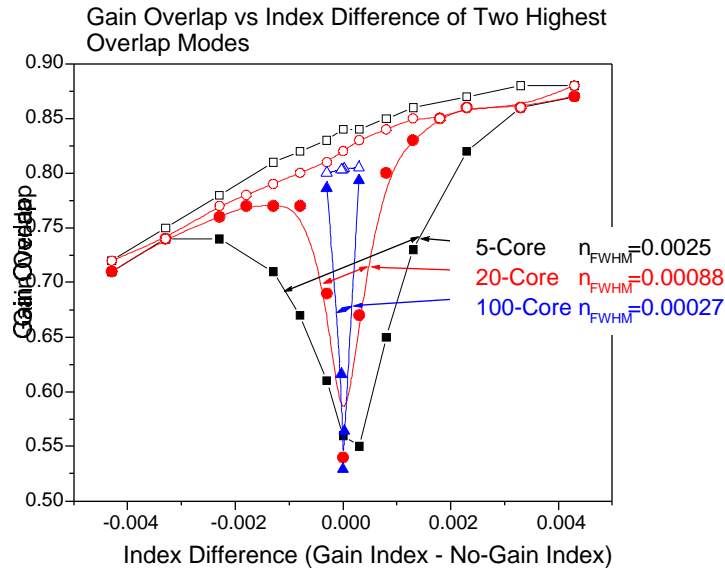
Figure 16 Overlap vs. Index Difference plot for one-dimensional structures having a systematic index variation between the gain and no-gain regions. Three different structures are investigated here consisting of 5, 20, and 100 cores, respectively. For each structure investigated, the gain overlap of the highest overlap and next highest overlap mode are plotted against the systematic index variation.
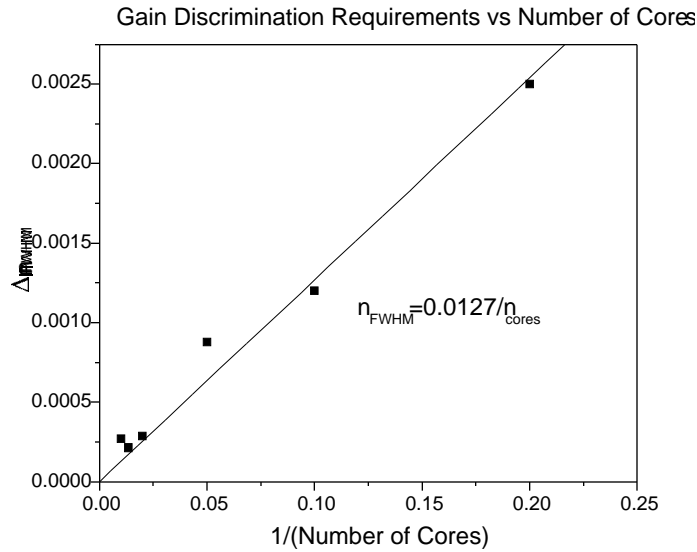

Figure 17 Gain discrimination requirements vs. the number of mode cores taken from the data in Fig. 16. Additionally, data points are included for a 10 gain-core, 50 gain-core and 75 gain-core structure. The FWHM spread in index plotted here is defined by the two points at which the gain discrimination between the two highest overlap modes just halves from its peak value at $\Delta n=0$. The straight line represents a linear least squares fit to the data points that is constrained to pass through the origin.

In addition to the systematic errors just considered, random variations in cell index and cell dimension may be an issue, particularly in fiber structures consisting of a large number of cells. To investigate the impact of random index variations we have modeled a 100-core ribbon fiber with nominally constant index throughout the waveguiding region. The particular one-dimensional waveguide design investigated here consists of a structure similar to the one of Fig. 10 but with cell dimensions of 3.65 μm for the central cells and 4.36 μm for the end cells. The impact of random variations in cell refractive index is illustrated in Fig. 18 where we have plotted the structure's eigenmode gain overlap against the various mode effective refractive indices. In each case, the individual cells that comprise the waveguide have had their refractive indices randomly varied with a uniform spread about the design point. The magnitudes of the uniform random distributions were taken to be $\delta n=0$, $\delta n=\pm 0.00015$, $\delta n=\pm 0.00037$, and $\delta n=\pm 0.00073$ as indicated. In Fig. 19, the overlaps of the two highest gain overlap modes for this structure are plotted as a function of the random error introduced in the individual cell refractive indices. Examining this plot, it is seen that the gain discrimination between the two highest overlap modes begins to substantially degrade when random index variations are approximately $\delta n=\pm 0.00037$, in approximate accord with the FWHM deduced in Figs. 16 and 17. We have also modeled the impact of random variations in the cell dimensions for the 100-core structure studied here and found in general it is very robust to these types of variations. Based on our modeling, random dimensional variations at the $\pm 10\%$ level do not significantly degrade the mode overlap and mode overlap discrimination and so are probably not an issue with the device fabrication.
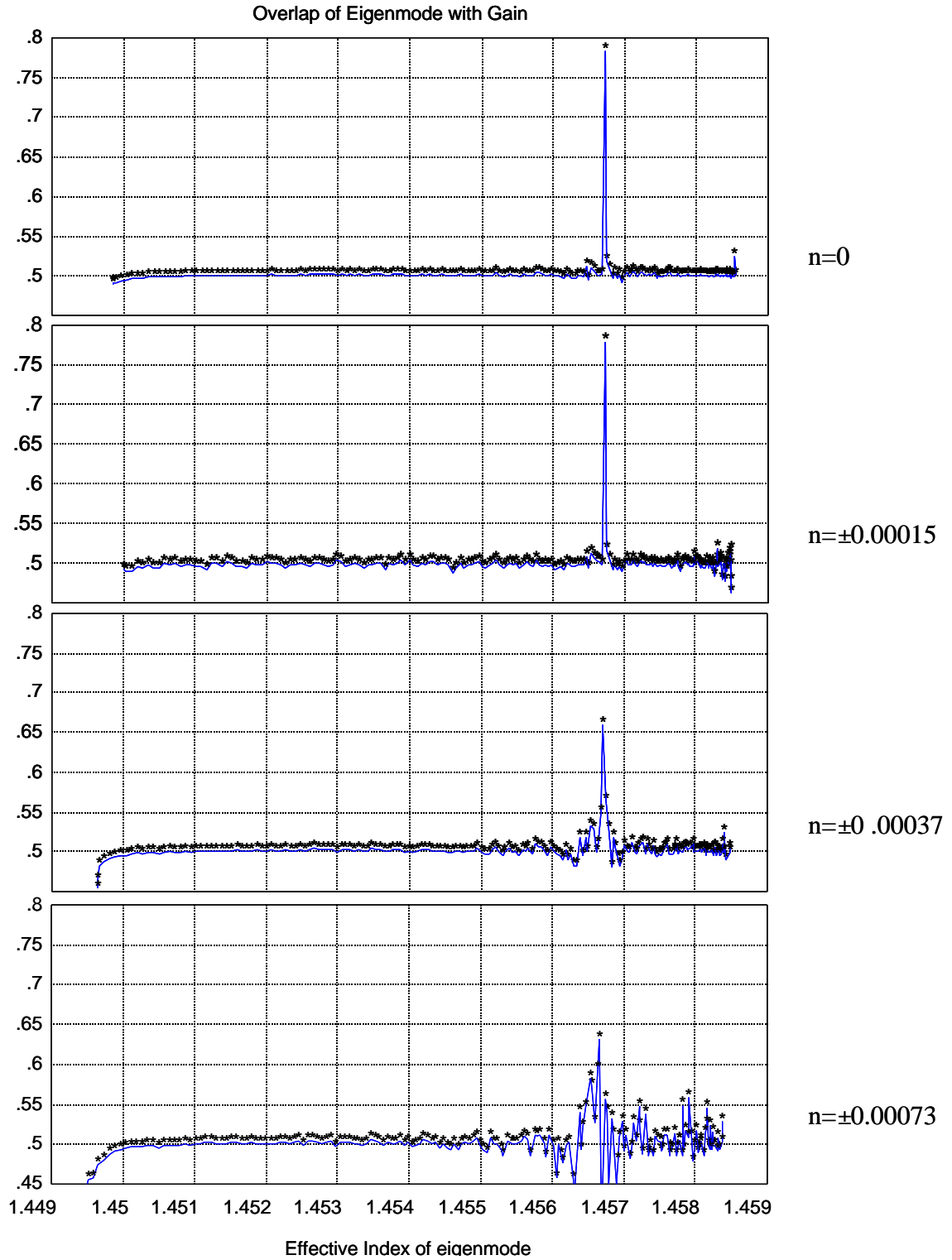
Figure 18 The impact of random variations in cell refractive index are illustrated here using a 100 core structure in which gain overlap of the structure's eigenmodes are plotted against the various mode's effective refractive index. In each case, the individual cells that comprise the waveguide have had their refractive indices randomly varied with a uniform spread about the design point. The magnitudes of the uniform random distributions were taken to be ∂n=0, ∂n=±0.00015, ∂n=±0 .00037, and ∂n=±0.00073 as indicated.
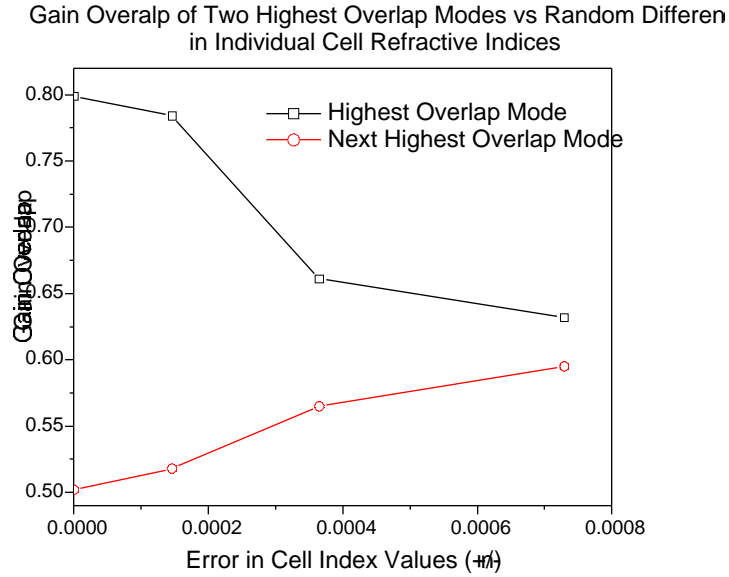
Figure 19 Gain overlap for 100-core ribbon fiber. The overlap of the two highest gain overlap modes from fig. 18 is plotted as a function of the random error introduced in the individual cell refractive indices. Random errors in refractive indices are uniformly distributed with the indicted amplitudes.

9. Conclusion

This paper describes a new, robustly scalable technique for phase locking multiple gain cores in a fiber structure based on anti-guiding or radiative coupling. Our focus has been on a ribbon-like geometry in which the waveguide region contains multiple gain cores alternating with non-gain regions in a periodic array. An outer, lower index cladding surrounds the entire ribbon structure. The distinguishing feature of our design is a constant refractive index profile across the waveguide region as opposed to alternating higher and lower index regions.   Our modeling predicts the constant index design will provide modes that meet our two critical design requirements: strongly favored oscillation in a single transverse mode and good intensity uniformity across the waveguide structure. The constant index case is also the most robust in terms of design tolerances that must be held with both the refractive index values across the waveguide region as well as physical dimensional tolerances.

References

[1] D. Botez and D. R. Scifres, <u>Diode Laser Arrays</u>, Cambridge Univ. Press 1994.

[2] W.J. Wadsworth, J.C. Knight, W.H. Reeves, P.St.J. Russell, and J. Arriaga, "Yb^{3+}-doped photonic crystal fibre laser," Electronics Letters 36, 2000.

[3] V. Dominic, S. MacCormack, R. Waarts, S. Sanders, S. Bricknese, R. Dohle, E. Wolak, P.S. Yeh, and E. Zucker, "110 W Fibre Laser," CLEO '99 Postdeadline Papers CPD11-1 and
V. Dominic, S. MacCormack, R. Waarts, S. Sanders, S. Bricknese, R. Dohle, E. Wolak, P.S. Yeh, and E. Zucker, "110 W Fibre Laser," Electronics Letters Vol. 35, No. 14, 1999.

[4] M. Muendal, B. Engstrom, D. Kea, B. Lalierte, R. Minns, R. Robinson, B. Rockney, Y. Zhang, R. Collins, P. Gavrolovic, and A. Rowley, "35-watt cw singlemode ytterbium fiber laser at 1.1 micron," Proc. CLEO, 1997, Post-Deadline Paper CPD30-1.

[5] H. Zeller, U. Willamowski, A. Tunnermann, H. Welling, S. Unger, V. Reichel, H.-R. Muller, J. Kirchof, and P. Albers, "High-Power cw neodymium-doped fiber laser operating at 9.2 W with high beam quality," Opt. Lett. 20, 578, 1995

[6] D. Meyhuys, K. Mitsunaga, L. Eng, W.K. Marshall, and A. Yariv, "Supermode control in diffraction-coupled semiconductor laser arrays," Appl. Phys. Lett. 53, p. 1165, 1988.

[7] P. Glas, M. Naumann, A. Schirrmacher, Th. Pertsch, "A cw diode-pumped single-silica fiber comprising 40 cores used as active elements for a high power fiber laser at 10 50 nm," CLEO '98 Technical Digest, paper CtuK5, p 113, Optical Society of America and
M. Wrage, P. Glas, M. Leitner, T. Sandrock, N.N. Elkin, A.P. Naprtovich, A.G. Sukharev, "Experimental and numerical determination of coupling constant in multicore fiber," Opt. Comm. 175, 97-102, 2000.

[8] Photonics Spectra October 2000, see report on Peter K. Cheo's evanescently coupled 7-core structure on page 20. This work is to be published in an upcoming Photonics Technology Letters article.

[9] M. Wrage, P. Glas, D. Fischer, M. Leitner, D.V. Vysotsky, A.P. Napartovich, "Phase locking in a multicore fiber laser by means of a Talbot resonator," Optics Letters, 25, 1436-1438, 2000.

[10] D. Mehuys, W. Streifer, R.G. Waarts, and D.F. Welch, "Modal analysis of linear Talbot-cavity semiconductor lasers," Opt. Lett. 16, 823-825, 1991.

[11] J. Banerji, A.R. Davies, and R.M. Jenkins, "Comparison of Talbot and 1-to-N-way phase-locked array resonators," Applied Optics, 36, 1604-1609, 1997.

[12] E.K. Gorton and R.M. Jenkins, "Theory of 1-N-way phase-locked resonators," Applied Optics, 40, 916-920, 2001.

[13] D. Botez and D. R. Scifres, <u>Diode Laser Arrays</u>, Cambridge Univ. Press 1994.

[14] D. Botez and A.P. Napartavich, "Phase-Locked Arrays of Antiguides: Analytical Theory," IEEE Journal of Quant. Elec. 30, 975-980, 1994
and
D.Botez, A.P. Napartovich, C.A. Zmudzinski, "Phase-Locked Arrays of Antiguides: analytic Theory II," IEEE Journal of Quant. Elec. 31, 244-253, 1995.

[15] T.M. Monro, D.J. Richardson, N.G.R. Broderick, and P.J. Bennet, "Holey Optical Fibers: An Efficient Modal Model," Journal of LightWave Technology, 17, p. 1093 , 1999.

[16] D. Marcuse, <u>Theory of Dielectric and Optical Waveguides</u>, Academic Press, New York (2nd ed. 1991).

[17] A.P. Napartovich and D. Botez, "Analytic theory of the strucure of collective modes in antiguided semiconductors," Quantum Electronics 26, 670-675, 1996
and
A.P. Napartovich and D. Botez, "Analytic theory of phase-locked arrays of antiguided diode lasers," SPIE Vol. 2994, Marek Osinski and Weng Chow Editors, 600-610, 1997.

[18] E. Yablonovitch, "Inhibitied spontaneous emission solid-state physics and electronics, Phys Rev. Lett. 58, 2059-2062, 1987.

[19] W.J. Wadsworth, J.C. Knight, W.H. Reeves, P.St.J. Russell, and J. Arriaga, "Yb^{3+}-doped photonic crystal fibre laser," Electronics Letters 36, 2000.

[20] J. Broeng, T. Sondergaaard, S.E. Barkou, P.M. Barbeito, and A. Bjarklev, "Waveguidance by the photonic bandgap effect in optical fibres," J.Opt. A: Pure Appl. Opt. 1, 477-482, 1999.

[21] D. Marcuse, <u>Theory of Dielectric and Optical Waveguides</u>, Academic Press, New York (2nd ed. 1991).

[22] M.D. Feit and J.A. Fleck, Jr., "A Spectral Approach to Optical Resonator Theory," Applied Optics **20**, 2843-51 (15 August 1981).

[23] M.D. Feit and J.A. Fleck, Jr., "Mode properties of optical fibers with lossy components by the propagating beam theory", Appl. Opt. **20**, 848-56 (1 March 1981).

[24] M.D. Feit and J.A. Fleck, Jr., "Computation of mode eigenfunctions in graded index optical fibers by the propagating beam method," Appl. Opt. 19, 2240-2246, 1980.

[25] M.D. Feit and J.A. Fleck, "Analysis of rib waveguide and couplers by the propagating beam method," JOSA A7, 73-79, Jan 1990.